MECHANISMS AND CRYSTAL CHEMISTRY OF OXIDATION IN ANNITE: RESOLVING THE HYDROGEN-LOSS AND VACANCY REACTIONS

D. G. RANCOURT[1], P. H. J. MERCIER[1], D. J. CHERNIAK[2], S. DESGRENIERS[1], H. KODAMA[3], J.-L. ROBERT[4] AND E. MURAD[5]

[1] Department of Physics, University of Ottawa, Ottawa, Ontario, Canada K1N 6N5
[2] Department of Earth and Environmental Sciences, Rensselaer Polytechnic Institute, Troy, New York 12180, USA
[3] Agriculture and Agri-Food Canada, 960 Carling Ave., Ottawa, Ontario, Canada K1A 0C6
[4] Centre de Recherches sur la Synthèse et Chimie des Minéraux, CNRS, F-45071 Orléans Cèdex 2, France
[5] Bayerisches Geologisches Landesamt, Aussenstelle Marktredwitz, Leopoldstrasse 30, Postfach 389, D-95603 Marktredwitz, Germany

Abstract—A synthetic octahedral-site-vacancy-free annite sample and its progressive oxidation, induced by heating in air, were studied by powder X-ray diffraction (pXRD), Mössbauer spectroscopy, nuclear reaction analysis (NRA), Raman spectroscopy, X-ray fluorescence (XRF) spectroscopy, gas chromatography (GC), thermogravimetric analysis (TGA), differential thermal analysis (DTA), scanning electron microscopy (SEM), and size-fraction separation methods. For a set heating time and as temperature is increased, the sample first evolves along an annite–oxyannite join, until all H is lost via the oxybiotite reaction (Fe^{2+} + OH^- $\rightleftharpoons$ Fe^{3+} + O^{2-} + H↑). It then evolves along an oxyannite–ferrioxyannite join, where ideal ferrioxyannite, $KFe^{3+}_{8/3}\square_{1/3}AlSi_3O_{12}$, is defined as the product resulting from complete oxidation of ideal oxyannite, $KFe^{3+}_2Fe^{2+}AlSi_3O_{12}$, *via* the vacancy mechanism ($3\ Fe^{2+}$ $\rightleftharpoons$ $2\ Fe^{3+}$ + $^{[6]}\square$ + Fe↑). A pillaring collapse transition is observed as a collapse of *c* near the point where $Fe^{2+}/Fe = \frac{1}{3}$ and all OH groups are predicted and observed to be lost. Quantitative analyses of H, using NRA, GC, and Raman spectroscopy, corroborate this interpretation and, in combination with accurate ferric/ferrous ratios from Mössbauer spectroscopy and lattice parameter determinations, allow a clear distinction to be made between vacancy-free and vacancy-bearing annite. The amount of Fe in ancillary Fe oxide phases produced by the vacancy mechanism is measured by Mössbauer spectroscopy to be 11.3(5)% of total Fe, in agreement with both the theoretical prediction of $\frac{1}{9} = 11.1\%$ and the observed TGA weight gain. The initiation of Fe oxide formation near the point of completion of the oxybiotite reaction ($Fe^{2+}/Fe = \frac{1}{3}$) is corroborated by pXRD, TGA, Raman spectroscopy, and appearance of an Fe oxide hyperfine field sextet in the Mössbauer spectra. The region of Fe oxide formation is shown to coincide with a region of octahedral site vacancy formation, using a new Mössbauer spectral signature of vacancies that consists of a component at 2.2 mm/s in the $^{[6]}Fe^{3+}$ quadrupole splitting distribution (QSD). The crystal chemical behaviors of annite–oxyannite and of oxyannite–ferrioxyannite are best contrasted and compared to the behaviors of other layer-silicate series in terms of *b vs.* [D] (average octahedral cation to O bond length). This also leads to a diagnostic test for the presence of octahedral site vacancies in hydrothermally synthesized annite, based on a graph of *b vs.* Fe^{2+}/Fe. The implications of the observed sequence of thermal oxidation reactions for the thermodynamic relevance of the oxybiotite and vacancy reactions in hydrothermal syntheses are examined and it is concluded that the oxybiotite reaction is the relevant reaction in the single-phase stability field of annite, at high hydrogen fugacity and using ideal starting cation stoichiometry. The vacancy reaction is only relevant in a multi-phase field, at lower hydrogen fugacity, that includes an Fe oxide equilibrium phase (magnetite) that can effectively compete for Fe, or when using non-ideal starting cation stoichiometries.

Key Words—Annite, Biotite, Crystal Chemistry, Differential Thermal Analysis, Ferrioxyannite, Gas Chromatography, Mössbauer Spectroscopy, Nuclear Reaction Analysis, Oxyannite, Oxybiotite, Scanning Electron Microscopy, Thermogravimetric Analysis, X-ray Fluorescence Spectroscopy.

INTRODUCTION

Ideal annite, $KFe_3AlSi_3O_{10}(OH)_2$, the hypothetical ferrous Fe end-member of the Mg-Fe solid-solution having Mg end-member phlogopite, $KMg_3AlSi_3O_{10}(OH)_2$, and Fe-rich member biotite, is a common model system for studying the Fe oxidation mechanisms of biotite. Synthetic annite is often used, although the ideal annite stoichiometry is never attained due to sheet mismatch structural constraints that require some Fe^{3+} to be present (Hazen and Wones, 1972, 1978). Proposed mechanisms for Fe oxidation in biotite include: the oxybiotite or oxyannite reaction, involving loss of structural H,
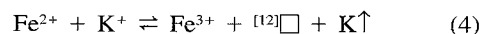
$$Fe^{2+} + OH^- \rightleftharpoons Fe^{3+} + O^{2-} + H\uparrow \tag{1}$$
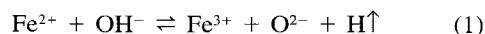
an Fe vacancy substitution, involving loss of structural Fe,

$$3\ Fe^{2+} \rightleftharpoons 2\ Fe^{3+} + {}^{[6]}\square + Fe\uparrow \tag{2}$$
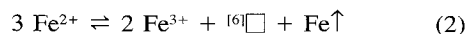
a change in Al/Si ratio, involving Al/Si substitution

$$Fe^{2+} + Si^{4+} + Al\uparrow \rightleftharpoons Fe^{3+} + Al^{3+} + Si\uparrow \tag{3}$$

and exfoliation by loss of interlayer K

$$Fe^{2+} + K^+ \rightleftharpoons Fe^{3+} + {}^{[12]}\square + K\uparrow \tag{4}$$

The first of these reactions is believed to play a dominant role in natural biotite, thereby allowing bi-

otite to form the basis of a widely used gauge of hydrogen (and oxygen) fugacity in igneous rocks, where the measured degree of Fe oxidation is related to the fugacity that prevailed during the most recent equilibration (Speer, 1984). It is also believed to play a major role during the re-equilibrations of biotite, associated with lava eruptions (*e.g.* Takeda and Ross, 1975).

The oxybiotite reaction is also used to interpret studies involving synthetic oxidation induced by heating biotite samples in air, where it is generally believed to be the dominant mechanism (Farmer *et al.,* 1971; Ferrow, 1987; Güttler *et al.,* 1989; Hogg and Meads, 1975; Ivanitskiy *et al.,* 1975; Rancourt *et al.,* 1993a; Rimsaite, 1970; Robert, 1971; Sanz *et al.,* 1983; Smith *et al.,* 1980; Tricker *et al.,* 1976; Vedder and Wilkins, 1969). This has been demonstrated most convincingly in the remarkable early work of Robert (1971) who resolved and examined the inter-relationships between (both thermally and chemically induced) ferrous Fe oxidation, structural H loss, interlayer cation exchange and hydration, and dehydroxylation ($2OH^- \rightleftharpoons \square + O^{2-} + H_2O\uparrow$), using a combination of methods including pXRD, TGA, DTA, elemental analysis, wet chemical ferrous Fe determination, optical microscopy, SEM and quantitative IR spectroscopy of both natural and deuterated samples. The oxybiotite reaction is also sometimes seen to be a dominant mechanism in laboratory oxidation of biotite samples using various wet chemical treatments (*e.g.* Robert, 1971; Ross and Rich, 1974). It is also believed to occur in the laboratory oxidation or re-equilibration of other Fe^{2+}-bearing and OH-bearing minerals (*e.g.* Borggaard *et al.,* 1982; Clowe *et al.,* 1988; Lear and Stucki, 1985; Veith and Jackson, 1974) and to represent a main mechanism of H incorporation in nominally anhydrous minerals such as pyroxenes (Skogby and Rossman, 1989; Skogby, 1994). On the other hand, in several studies of natural and laboratory weathering of biotite, the vacancy mechanism is seen to dominate (*e.g.* Gilkes *et al.,* 1972a; Goodman and Wilson, 1973; Robert, 1971; Wilson, 1970). Also, there is evidence (Bouda and Isaac, 1986) that the Eh-controlled oxidation of biotite in soils may predominantly occur via K loss (reaction 4). An overview of thermally induced oxidation in clay minerals was given by Brindley and Lemaitre (1987).

Early workers (Eugster and Wones, 1962; Wones, 1963) concluded that the main relevant reaction in synthesizing annite and biotite samples was the oxybiotite reaction and that it was necessary to postulate an oxyannite end-member. In opposition to this, Rebbert *et al.* (1995) reported that the dominant mechanism in a series of synthetic samples oxidized under hydrothermal conditions is the vacancy mechanism (reaction 2) and have suggested that the vacancy mechanism may be more prevalent in natural settings than previously thought. Their conclusions were sup-

ported by wet chemical determinations of ferric/ferrous ratios, quantitative H determinations, and accurate lattice parameter measurements. Redhammer *et al.* (1993) also concluded that the dominant oxidation mechanism in hydrothermally synthesized annite is the vacancy mechanism, based on an interpretation of infrared (IR) spectra that has been contested by Rancourt *et al.* (1994a). Virgo and Popp (2000) performed a detailed study of the oxidation and H-loss mechanisms in mantle-derived phlogopites (including 40 synthetic re-equilibrations) and have re-examined the conclusions of Rebbert *et al.* (1995), of Redhammer *et al.* (1993), and of researchers who analyzed ferric/ferrous and H contents in natural micas (Feldstein *et al.,* 1996; Feeley and Sharp, 1996). In opposition to the suggestions of Rebbert *et al.* (1995), they have shown that the Fe^{3+} in their natural phogopites occurs exclusively via the oxybiotite reaction (reaction 1) and that this interpretation is consistent with all considered published data on natural samples, where quantitative ferric/ferrous and H analyses were available. Although they questioned the conclusions of Rebbert *et al.* (1995) and of Redhammer *et al.* (1993) concerning synthetic annite, they also admitted the possibility that the Fe end-members may have a different oxidation mechanism. On the other hand, Mercier *et al.* (1996, 1999) found that the variations in $^{[6]}Fe^{3+}$, $^{[4]}Fe^{3+}$ and $^{[6]}Fe^{2+}$ site populations caused by changing hydrothermal synthesis conditions for annite occur without the presence or formation of octahedral vacancies. Ferrow and Annersten (1984) stressed that the chemistry of the system (*e.g.* chemical potentials of Al and K) plays a dominant role in the oxidation of annite under hydrothermal conditions. These various results again bring up the obvious relevant questions: (1) Under which conditions do the possible mechanisms dominate or coexist? (2) Can this be understood in terms of simple crystal chemical and thermodynamic or kinetic considerations? The difficulty in answering the first question (or even in simply distinguishing the different reactions) lies in the difficulties related to quantifying H, vacancies, and ferric and ferrous Fe site populations. Indeed, the present study is only the second study (after Rebbert *et al.,* 1995) in which synthetic micas have been studied and both quantitative H and ferric/ferrous evaluations have been used.

SAMPLE SYNTHESIS AND TREATMENT

The starting sample was the same synthetic annite sample that has previously been described and characterized in detail by cryogenic and ambient temperature ^{57}Fe Mössbauer spectroscopy, high-field and low-field magnetometry, pXRD, SEM and IR (Rancourt *et al.,* 1994a, 1994b). The original synthesis yielded a large amount of product (10 g) and was not synthesized as previously incorrectly stated (Rancourt *et al.,* 1994a) but rather as follows. A hot-seal Morey-

Table 1. Refined lattice parameters.

| Sample	N.Rl.[1]	a (Å)	b (Å)	c (Å)	β (°)	Vol. (Å³)
ASIS-W-r	31	5.3944 (7)	9.341 (1)	10.319 (3)	100.04 (2)	512.0
ASIS-L-r	32	5.393 (1)	9.342 (1)	10.317 (1)	100.04 (1)	511.8
ASIS-S-r	32	5.393 (1)	9.3426 (5)	10.321 (1)	100.04 (1)	512.1
250-5-W-m	31	5.3878 (2)	9.333 (2)	10.314 (2)	100.04 (2)	510.7
300-5-W-m	30	5.380 (1)	9.320 (1)	10.297 (4)	100.04 (3)	508.4
350-5-W-m	24	5.3580 (8)	9.279 (2)	10.256 (2)	100.02 (2)	502.1
350-5-W-k	23	5.361 (1)	9.286 (1)	10.263 (1)	100.05 (2)	503.1
370-5-W-k	23	5.3338 (8)	9.241 (1)	10.135 (2)	100.10 (2)	491.8
400-5-W-m	29	5.3125 (8)	9.198 (2)	10.140 (2)	100.04 (2)	487.9
450-5-W-m	30	5.3080 (8)	9.196 (1)	10.139 (2)	100.04 (2)	487.3
500-5-W-m	31	5.3076 (6)	9.194 (1)	10.130 (2)	100.06 (1)	486.7
550-5-W-m	31	5.3068 (8)	9.191 (2)	10.131 (2)	100.05 (2)	486.6
600-5-W-m	31	5.3065 (9)	9.192 (1)	10.124 (3)	100.06 (2)	486.2

[1] N.Rl.: number of reflections used in the refinement.

type autoclave having an internal volume of 44 cm³ was used in which the ~10 g of stoichiometric starting gel was sealed in a silver tube and the correct amount of water was added to produce a synthesis pressure of 1 kbar at the synthesis temperature of 600°C. The relatively large amount of water (~14 cm³) can take up a considerable amount of dissolved K. In order to ensure K stoichiometry of the annite product, therefore, the water was actually replaced by a 2 M solution of K, as KCl. This gave rise to a certain amount (~10 wt.%) of KCl impurity phase in the dry product that is described below and that does not otherwise affect the synthesis since Cl is not easily incorporated into mica structures (Volfinger *et al.*, 1985).

No impurity phases were detected in any of several high-quality pXRD scans of the starting material, except KCl that arises from precipitation from the synthesis solution, as explained above. All other detected lines were indexed to 1*M*-polytype annite, in accordance with the simulated diffraction pattern for this assumed structure. The KCl impurity was also detected by SEM combined with energy dispersive X-ray spectroscopic (EDS) microprobe analysis, as relatively large crystals (~10 μm). No other impurity phases were detected by SEM and EDS. No Fe-bearing impurities were detected in any of the high-quality Mössbauer spectra collected both above and below the magnetic ordering temperature (58 K) of the synthetic annite sample. Neither were Fe-bearing impurity phases detected by low-field superconducting quantum interference device (SQUID) magnetometry which is extremely sensitive to the presence of oxides such as magnetite, hematite and maghemite. It was argued that this sample did not contain octahedral site vacancies, based on the value of the Curie constant from magnetometry and the absence of a vacancy (V) band in IR (Rancourt *et al.*, 1994a). This is corroborated by the measurements reported below, including accurate total-H determinations performed by both NRA and GC. The large starting weights used

and the absence of detectable impurity phases set stringent constraints on the resulting composition of the product material that we believe is as close to the ideal K:Fe:Al:Si:O = 1:3:1:3:12 as possible. Except for K because of the KCl impurity described above, this ideal stoichiometry is corroborated by accurate XRF measurements that are described below. We also found no detectable signs of sample inhomogeneity, except for small differences in ferric and ferrous Fe-site populations in the large (L) and small (S) size-fractions ($d > 1$ μm and $d < 1$ μm, as defined below) that do not give rise to measurable associated small differences in lattice parameters (Table 1).

Accurate site populations of $^{[6]}Fe^{3+}$, $^{[4]}Fe^{3+}$ and $^{[6]}Fe^{2+}$ have been determined previously for the starting synthetic annite sample and were found to be 7.0(2), 4.0(2) and 89.0(2)% of total Fe, respectively (Rancourt *et al.*, 1994a). Using the fact that no vacancies can be detected and assuming that the $^{[4]}Fe^{3+}$ occurs *via* the usual Al/Fe exchange, $^{[6]}Fe^{3+} + {}^{[4]}Al^{3+} \rightleftharpoons {}^{[4]}Fe^{3+} + {}^{[6]}Al^{3+}$, implies that all the ferric Fe has occurred *via* the oxybiotite reaction (reaction 1) and that the stoichiometric crystal chemical formula of the starting annite sample should be written as:

$$\{K^+\}[Fe^{2+}_{3-x-y}Fe^{3+}_x Al^{3+}_y]\langle Al^{3+}_{1-y}Fe^{3+}_y Si^{4+}_3\rangle$$

$$O^{2-}_{10+x+y}(OH^-)_{2-x-y} \qquad (5)$$
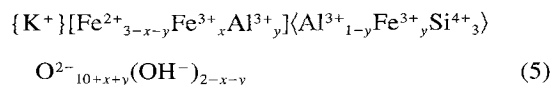
where $x = 3^{[6]}Fe^{3+}/Fe = 0.210(6)$, $y = 3^{[4]}Fe^{3+}/Fe = 0.120(6)$, and $\{\}$, $[\ ]$ and $\langle \rangle$ represent inter-layer, octahedral and tetrahedral sites, respectively. The total H calculated thus is in quantitative agreement with accurate determinations of total H obtained by both NRA and GC that are described below, thereby providing further strong support for the conclusion that there were no vacancies present in the starting annite.

This sample was also the starting sample in a study that involved re-equilibrating under hydrothermal conditions with the C-CH₄ buffer at various temperatures within the stability field of annite and that found that

x and *y* vary as predicted from a crystal chemical model that takes inter-sheet mismatch, octahedral flattening, tetrahedral rotation, tetrahedral elongation along *c,* and different thermal expansion coefficients for tetrahedral and octahedral bonds into account, with no evidence of vacancies or vacancy formation (Mercier *et al.,* 1996, 1999).

The oxidized annite samples were prepared by heating small amounts (typically 20–100 mg) of the original synthesis product in air at different set temperatures for 5 h (or 30 min in one case). The quench was accomplished by simply pulling the sample and its open-ended quartz tube holder out of the furnace. The resulting quench rate is not expected to affect the results significantly, given what is known about the kinetics of the relevant reactions. The oxidized annite samples are referred to as *XXX-Y-Z*-M, where: *XXX* is the treatment temperature (°C), *Y* is either 5 (for a treatment time of 5 h) or 30 (for a treatment time of 30 min), *Z* refers to the original material size-fraction used (W = whole sample = all size fractions; S = small sizes, *d* < 1 μm; L = large sizes, *d* > 1 μm), and M is a letter identifying the particular sample since certain treatments with identical conditions were repeated. In the case of the original untreated annite starting material, *XXX-Y* is replaced by 'ASIS', to mean 'as-is'.

For experiments where part of the original powder sample was separated into *d* < 1 μm and *d* > 1 μm size-fractions (referred to as the S and L fractions, respectively), fractionation was achieved by a sedimentation method using acetone instead of water, under anoxic and dry conditions. The use of acetone greatly reduces the settling time and allows drying by simple evaporation. The two size-fractions were examined by SEM and found to be well separated, with the S fraction being 20% of the original mass of 810 mg and having only sizes in the range 0.1–1.0 μm whereas the L fraction had the remaining larger crystals with sizes 1–3 μm and fewer crystals in the *d* < 1 μm range compared to the unseparated sample, by a factor of ~2. The L and S fractions were characterized separately and used to make oxidized annite samples by heat treatments, which were also characterized.

EXPERIMENTAL METHODS AND DATA ANALYSIS

Powder X-ray diffraction

Most of the pXRD patterns (*i.e.* those measured at the University of Ottawa) were collected using an automated Philips X'Pert PW3710 system twin-goniometer θ–2θ powder diffractometer, using CuKα radiation with a variable divergent slit and either a graphite crystal secondary beam monochromator with gas-filled proportional detector or a Kevex solid-state detector having sufficient energy resolution to select only the CuKα radiation. Samples were mounted as acetone smears on a single-crystal silicon wafer low-background holder that either spun (on the Kevex side) or was stationary (on the graphite crystal side).

Lattice parameters were refined using 23–32 reflections with the refinement program of Appleman and Evans (1973). Care was taken to best estimate the CuKα$_1$ position of each reflection and to use the corresponding CuKα$_1$ wavelength in the refinement. The estimated error in angular position of a reflection was 0.02°2θ. The stated errors in lattice parameters are standard deviation errors evaluated by a synthetic method using a Gaussian error width of 0.02°2θ on all line positions and 100 different line position data sets generated for each lattice parameter refinement. This gave typical standard deviation errors of ±0.001 Å in *a, b* and *c* and ±0.02° in β.

Mössbauer spectroscopy

Room temperature (RT = 22°C) ^{57}Fe Mössbauer spectra were collected in transmission mode using random orientation powder absorbers having 5–85 mg of dry sample per cm^2 in holders with ½ inch or ⁵⁄₁₆ inch diameter windows. The calculated ideal absorber thickness for ideal annite is 38 mg/cm^2 (Rancourt *et al.,* 1993b), corresponding to a Mössbauer thickness parameter of *t* = 5.1 when the absorber recoil-less fraction is assumed to be f$_a$ = 0.7; consequently, this thickness was used most often. Thicker absorbers were also used to test for the absence of texture and thickness non-uniformity problems. Thinner absorbers (5–10 mg/cm^2) gave evident texture and absorber thickness non-uniformity problems but ideal thickness and thicker absorbers showed no such effects. Another successful absorber configuration involved 30 mg/cm^2 of annite powder and either five times as much benzophenone or nine times as much finely ground sugar. Calibration was obtained using an enriched ^{57}Fe foil at RT and all center shifts (CSs) are reported with respect to the CS of metallic Fe at RT. The transducer was operated in constant acceleration mode or in sinusoidal mode and folding was performed to achieve a flat background. All samples were measured with two velocity ranges: ±11 mm/s in order to detect any magnetically split oxides and on an expanded velocity range of ±4 mm/s in order to obtain the best possible resolution in the resonance region of annite.

Rancourt (1994a, 1994b) and Rancourt *et al.* (1994c) showed that the usual methods of fitting chemically disordered paramagnetic-state minerals with Lorentzian doublets representing the crystallographic sites are too coarse an approximation for most quantitative work and that the correct method involves extracting generalized-site-specific quadrupole splitting distributions (QSDs). All Mössbauer spectra were fitted with the Voigt-based fitting method of Rancourt and Ping (1991) for QSDs and simultaneous hyperfine

field distributions (HFDs) when Fe-oxide phases were present, using the Recoil software of Lagarec and Rancourt (1998). See Rancourt and Ping (1991) for all Mössbauer parameter definitions and a detailed description of the relevant notation.

Since accurate Fe-site populations were required in this application and since correct QSDs were also desired, it was necessary to perform full absorber thickness corrections. We used the procedure of Rancourt (1989, 1996) that is implemented in Recoil. This involves generating a synthetic thin-limit spectrum using the raw folded data, that is completely corrected for absorber thickness effects, both spectral shape and relative and absolute intensities. Such corrected spectra are then analyzed in the same way as the raw folded spectra, using QSDs and HFDs. The only required user-supplied parameter for this exact correction is the average recoil-less fraction of the absorber material (Rancourt et al., 1993b). This recoil-less fraction has been measured to be $f_a = 0.5$ for synthetic annite (Royer, 1991; Rancourt et al., 1994a), which is the value we used. It is important to note that the calculated corrected spectrum is not sensitive to the precise value of f_a, where, for example, $f_a = 0.7$ gives the same results within experimental error. We find that thickness effects cause systematic errors of several percent or more in site populations, whereas we require an accuracy of ~0.2%.

Another main concern in obtaining accurate site populations from Mössbauer spectroscopy is the possibility that the site-specific or cation-species-specific recoil-less fractions may not be equal, for a given sample (Rancourt, 1989). It has often been suggested that the recoil-less fractions for ferric and ferrous Fe may be substantially different. For example, this seems to be the case in the data presented by De Grave and Van Alboom (1991), though one should note that the latter data compare the average recoil-less fractions of minerals that predominantly contain either ferric or ferrous Fe and that they do not address the question of cation-species-specific recoil-less fractions in a given sample. In a recent detailed comparative study of Mössbauer spectroscopy and wet chemical methods, using several biotite samples including some geochemical standards, Lalonde et al. (1998) found that the ratio of ferric to ferrous recoil-less fractions at RT in any given sample was close to one, $f_{3+}/f_{2+} = 1.009(5)$. All the samples in the latter study contained only $^{[6]}Fe^{3+}$ and one might ague that stiffer tetrahedral Fe–O bonds should give rise to larger $^{[4]}Fe^{3+}$ recoil-less fractions. Rancourt et al. (1994a) addressed this question for synthetic annite by comparisons with Mössbauer spectra measured at liquid helium temperature (4.2 K) where the spectral contributions are magnetically hyperfine split and the $^{[6]}Fe^{3+}$ and $^{[4]}Fe^{3+}$ spectral contributions are resolved as separate lines. They found that the recoil-less fractions for $^{[6]}Fe^{3+}$, $^{[4]}Fe^{3+}$ and $^{[6]}Fe^{2+}$ were equal within exper-

imental error at temperatures in the range 4.2–300 K, in the same synthetic annite sample that we have used as our starting material. Given the situation described above, we have assumed that all the site-specific and cation-species-specific recoil-less fractions are equal in each of our oxidized annite samples, as well as in our starting as-synthesized sample. We also assume that the recoil-less fractions of the $^{[6]}Fe^{3+}$ in the Fe oxide phases that are produced at the highest treatment temperatures are all the same and equal to the assumed equal recoil-less fractions of the annite and oxidized annite samples.

Nuclear reaction analysis

The H concentrations were measured at the Dynamitron accelerator at the State University of New York at Albany with resonant nuclear reaction analysis, using the nuclear reaction $^{15}N + ^1H \rightarrow ^{12}C + ^4He + \gamma$ (Lanford et al., 1976). This reaction has a large cross-section at a ^{15}N beam energy of 6.385 MeV. An incident beam of $^{15}N^{++}$ was used, with the γ rays produced in the reaction detected by a bismuth germanate (BGO) scintillation detector positioned ~2 cm behind the samples. The chamber also contains a filament to neutralize charge build-up during the analysis of insulating materials, as described elsewhere (Lanford, 1995).

The samples were formed by pressing (~10 MPa pressure) the annite powder to 4 mm disks (~0.5 mm thick) in a small die. After pressing, pellets were either transferred to a desiccator directly or dried for a few hours in a drying oven (~100°C), then stored in a desiccator until analyzed. For analysis, the samples were mounted on a glass slide, affixed with a small drop of epoxy or double-sided carbon tape. The slide was mounted with vacuum grease on a Cu plate in a rotatable sample wheel chamber modified for cold analysis (e.g. Schnatter et al., 1988). The Cu plate was connected to a Cu rod, which extends through a vacuum seal on the chamber and out to a dewar of liquid nitrogen outside the chamber to help keep the samples cold during analysis. After mounting, the samples and copper plate were pre-cooled by spraying with liquid nitrogen. The chamber was then attached to the beamline and vacuum system and pumped down for hydrogen analysis.

Incident beam energies from 7.0 to 7.8 MeV were used, corresponding to depths in the annite material of 290 to 680 nm. Because of concerns about H loss during very long acquisition times on a single spot, data were taken by collecting a series of brief analyses on a single spot and monitoring count rates for a given amount of live charge delivered to the target. These were then summed and considered to be a single analysis (the beam was not moved during the entire integrated acquisition time, and there were no significant time gaps between successive acquisitions). Analyses

made on different spots on the sample surface at a given energy and at different energies on the same spot were considered separately. Backgrounds were taken by recording the number of counts detected in the windowed energy region of interest in the multi-channel analyzer with the beam blocked. This then provided the number of background counts expected during times of data acquisition. Calculated errors are based on counting statistics; backgrounds are incorporated into error propagation (assuming uncorrelated errors) in the usual way, *i.e.* $s = (x^2 + b^2)^{1/2}$, where x is the total number of counts in the windowed energy region of interest (centered on the 4.43 MeV γ ray), and b is the number of background counts expected for the data acquisition time.

The H concentration (C = number of H atoms per cm^3 of annite material) is related to the γ ray yield (Y = number of counts per unit of incident ^{15}N) as:

$$C = K(dE/dx)Y \qquad (6)$$

where K is a constant incorporating reaction cross-section parameters and characteristics of the analysis geometry that do not depend on sample characteristics and dE/dx is the stopping power for ^{15}N in annite, at the particular beam energy (Lanford, 1995). The validity of this formula is not altered by a powder sample morphology in which powder grains are separated by vacuum, although it becomes impossible to do accurate depth profiling of the H concentration. The largest accuracy limiting uncertainty in determining C is related to dE/dx. The values of dE/dx were calculated for annite (using the calculated mass density) using the latest version of the software developed by Ziegler *et al.* (1985) and Ziegler and Biersack (2000) and are believed to be accurate within 1–2%. The values were 2.19 and 2.20 MeV/μm for 7.8 and 7.0 MeV beam energies, respectively.

The H quantification by NRA reported here may be the first such analysis on a rock-forming mineral and, to our knowledge, is the first such analysis on a clay-size synthetic mineral. Extensive tests were performed on pressed pellets of the starting annite sample, both that had been heated to drive off sorbed water and that had not been heated. In this way, we were able to establish that, for a series of sequential analyses on the same spot, a first relatively small and relatively rapid decrease in H concentration was due to the loss of sorbed water. This was followed by a plateau of H concentration values that extended for 10 or more spot analyses at the same spot, after which the H concentration value started dropping, on further analyses on the same spot. The latter drop was interpreted as being an artifact of beam-induced (thermal) damage and was seen to be significantly less under cold conditions, relative to simple RT measurements. Plateau values were always recovered on either changing spot location or going to a larger penetration depth by increasing the

beam energy. All reported values are from analyses taken on the plateau and therefore correspond to intrinsic structural H concentrations.

Raman spectroscopy

Unpolarized Raman spectra were recorded on a Jobin-Yvon S3000 spectrometer equipped with a liquid nitrogen cooled detector using continuous wave 488.0 nm radiation. All spectra were recorded at 5 cm^{-1} resolution and were not corrected for the instrument spectral response. Raman shifts are accurate within 1 cm^{-1}. The incident laser light was focused on the powder samples to a spot size of 40 μm in diameter and light was collected in a near-backscattering geometry. Laser powers at the sample were kept below 5 mW to avoid heating and possible modification of the samples. Integrated Raman intensities were typically obtained by profile fitting using one or more Lorenztian lines with a linear background in a region of interest. Raman intensities were normalized by calculating the ratio of the integrated intensity of Raman lines of interest to those of Raman lines not or negligibly affected by the dehydration or oxidation reactions of the annite samples. For normalization purposes we chose the Raman lines centered at 843, 896 and 1296 cm^{-1}, which probably correspond to modes involving O–O bonds and O–M bonds (M = Al, Si, Fe, on tetrahedral sites) or O–M (M = Fe, Al, on octahedral sites) (*e.g.* McKeown *et al.*, 1999). It should also be noted that an increase of photo-induced luminescence was recorded with the increase of the treatment temperature.

X-ray fluorescence spectroscopy and gas chromatography

The XRF elemental analyses were obtained using a Philips PW2400/00 sequential X-ray spectrometer. Because of limited sample amounts, an XRF analysis was performed only for the starting annite. For this purpose a new calibration was developed that used only 250 mg of sample in preparing fused disks with 4.0750 g of flux material (3.2000 g Li$_2$B$_4$O$_7$; 0.8750 g LiBO$_2$). The new calibration was based on a complete suite of international standards. Precision was evaluated by performing several analyses on the same fused disk and was found to be 0.01 wt.% or better (error in the mean) for the relevant major oxides (Fe$_2$O$_3$, SiO$_2$, Al$_2$O$_3$ and K$_2$O). Accuracy was evaluated by measuring five relevant standards, that had not been used in establishing the calibration, and was estimated (average absolute deviations) to be 0.2, 0.3, 0.1 and 0.01 wt.% for Fe$_2$O$_3$, SiO$_2$, Al$_2$O$_3$ and K$_2$O, respectively.

Light element analyses (C, H, N, S) were obtained by GC of combustion products using thermal conductivity (thermistor) detection with a CE Instruments model EA-1110 elemental analyzer. Quantification was achieved by using time-integrated thermistor signals and corresponding run-specific calibrations for C,

H, N and S. Several standards (typically 10–20) were run before, during, and after the measurements, that were used to construct a calibration curve for each element. The calibration curves were found to be linear, within the precision of 0.01 wt.% or better, and were constrained to intersect with the origin in order to avoid systematic errors at the smallest measured values. Detection limit and accuracy were evaluated from the distributions of repeated values for standards and were found to be 0.01 wt.% or better for all elements, including H. All relevant factors that can affect the integrated signals were evaluated, including: sorbed water on the Sn combustion capsule; sorbed water on the sample itself; sorbed water on the standards; sorbed water on the V_2O_5 combustion agent when used; and the errors in evaluating the integrated signals. A number of measurements (10) of the untreated annite were performed, using samples weights in the range ~0.1 to 5 mg, both with and without V_2O_5. Sorbed water was typically removed by heating at 105°C for different times of the order of 1 h. Details of this method and examples of applications to natural and synthetic layer silicates will be reported elsewhere.

Other methods: TGA, DTA and SEM

Thermogravimetric analysis was first performed at the Institute for Research in Construction, National Research Council, on a DuPont 9900 thermal analyzer, both under air and dry N_2 gas, using an initial weight of ~100 mg, a heating rate of 20°C/min, an air flow rate of 100 ml/min or an N_2 flow rate of 150 ml/min. Differential thermal analysis was also performed on the same DuPont 9900 system, using ~30 mg of sample, under both air and dry N_2 gas, with the same heating rate and gas flow rates as with the TGA. Another TGA measurement was then performed on a TA Instruments TGA151 system at the Institute for Chemical Process and Environmental Technology, National Research Council, under air, using ~10 mg of sample and a lesser heating rate of 2°C/min.

Scanning electron microscopy was performed on a JEOL JSM 6400 system on carbon-coated loose powder mounts at the Research Facility for Electron Microscopy, CURFEM, Carleton University, Ottawa. The EDS X-ray microprobe analysis was used to look for and identify impurity phases.

MAIN RESULTS

Powder X-ray diffraction

The refined lattice parameters are given in Table 1. When b is plotted as a function of a, one finds a straight line relationship with a slope of $\sqrt{3}$, that is valid for all degrees of oxidation and that is the same as that obtained for several synthetic solid-solution series. This is shown in Figure 1 where the values for

our annite and oxidized annite samples are compared to those for the samples of Fe-Ni, Fe-Mg, Co-Mg, Ni-Mg and annite-fluorannite synthetic true trioctahedral mica solid-solutions that are described by Mercier (2001). While this relationship is not imposed by any of the known space groups for mica, it is a direct consequence of the hexagonal in-plane pseudo-symmetry of an octahedral sheet and it is expected to hold exactly to the extent that this pseudo-symmetry is not broken by some feature such as chemical order, for example. We have found that the few exceptions where this relationship (Figure 1) did not appear to hold for a particular synthetic sample could always be traced to an error in indexing one or more of the reflections or to an error in tabulating one or more of the peak positions. In practice, therefore, agreement with the relationship illustrated in Figure 1 is valid evidence that a lattice parameter refinement has been done correctly.

We have examined all of the pXRD patterns for any impurity phases that may occur in the samples that were heat treated. The KCl impurity described above gives rise to detectable KCl reflections at d-spacings of 3.14, 2.22, 1.82, 1.57, 1.41 and 1.28 Å in all the samples, *i.e.* the original KCl impurity of the starting material appears to be an inert phase that is not affected by any of the heat treatments, up to 600°C. No other impurity phases were detected in any of the samples treated at 250, 300 and 370°C. The samples treated at 350°C (350-5-W-m and 350-5-W-k) gave different results: 350-5-W-k showed small unidentified reflections at d-spacings of 3.52 and 3.50 Å that were not present in 350-5-W-m, and 350-5-W-m showed a single impurity reflection at d-spacing 3.03 Å which is attributed to KO_2 and that was not present in 350-5-W-k. The sample treated at 400°C showed only a single impurity phase reflection at d-spacing 1.69 Å that is attributed to hematite, in addition to the KCl impurity reflections. The diffractograms of all samples treated at 450, 500, 550 and 600°C contained a reflection at d-spacing 3.03 Å that is attributed to KO_2 and reflections at d-spacings 2.70, 2.50, 2.19 and 1.69 Å that are attributed to hematite. Note that the reflection attributed to KO_2 is the strongest reflection of this structure (Carter *et al.*, 1952) and that it cannot be due to the only other likely candidate, maghemite, because this strong reflection in maghemite and in Al-substituted maghemite samples always occurs in the d-spacing range 2.94–2.97 Å.

Estimated weight ratios of the impurity phases described above relative to the weight of annite can be calculated using reference intensity ratios (RIRs) for the specific reflections (Hubbard and Snyder, 1988), assuming an absence of texture, and the results are given in Table 2. Here, the chosen reflections for integrated intensity evaluations were: 001 annite, 222 KCl, 200 KO_2, and 116 hematite. Other useable re-
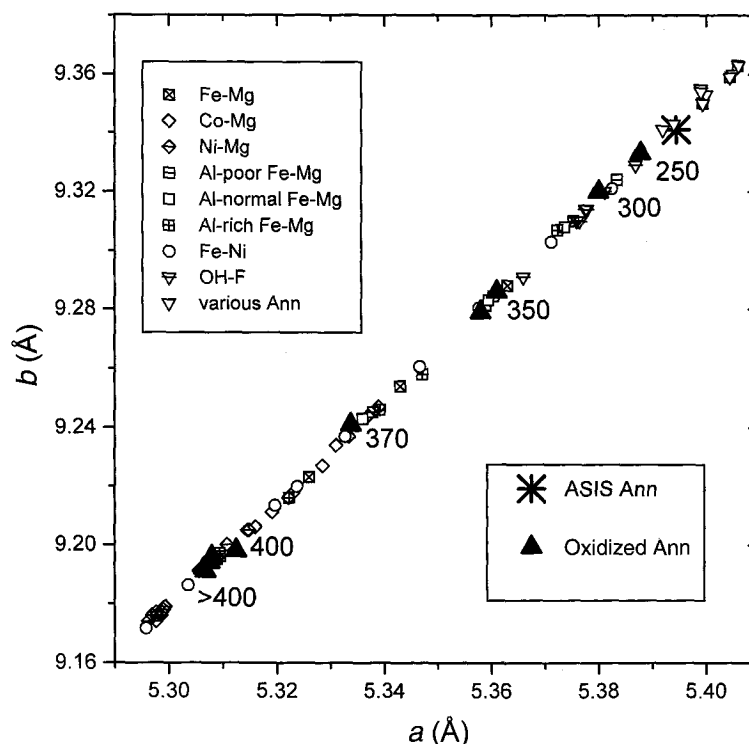
Figure 1. *b vs. a* for the starting annite sample and for the oxidized annite samples (treatment temperatures as indicated, in °C, compared to values for several other synthetic mica samples: various Fe-Mg series, a Co-Mg series, a Ni-Mg series, an Fe-Ni series, various synthetic annite samples, and an annite-fluorannite series (Mercier, 2001).

Table 2. Quantification of impurity phases detected by pXRD[1].

Sample	KCl/annite	KO$_2$/annite	Hematite/annite
ASIS-W-r	6	—	—
ASIS-L-r	9	—	—
ASIS-S-r	—[2]	—	—
250-5-W-m	10	—	—
300-5-W-m	13	—	—
350-5-W-m	—[3]	0.5[3]	—
350-5-W-k[4]	10	—	—
370-5-W-k	18	—	—
400-5-W-m	19	—	5
450-5-W-m	7	1.2	4
500-5-W-m	14	0.6	7
550-5-W-m	8	0.8	7
600-5-W-m	10	0.2	9

[1] Expressed as weight ratios, in %. Detection limit is better than 0.1%.

[2] The d <1 μm size-fraction did not contain any KCl, as confirmed by SEM.

[3] This sample was treated with chloroform to remove Mössbauer absorber grease. This treatment apparently removed the KCl and caused some KO$_2$ formation.

[4] As noted in the text, this sample also contained unidentified impurity reflections at 3.52 and 3.50 Å.

flections gave the same results within error. In the case of KO$_2$, a measured RIR is not given in the Powder Diffraction File (PDF). Therefore, we used a theoretical method based on calculated form factors and material densities for the ideal structures (Chung, 1974a, 1974b). When used with the other detected impurity phases (hematite and KCl), the latter theoretical method gave the same results within a factor of two (smaller). This degree of agreement is good, given the uncertainty in the measured RIR for annite. In fact, a measured RIR for synthetic annite is not available. We used a value of 4.0 (relative to the accepted corundum standard), based on published values for natural phlogopite and biotite samples, that vary over a wide range (Davis *et al.*, 1990). We applied corrections for our automatic divergent slit configuration. These methods also require that the usual Lorentz polarization factor corrections be applied to the integrated intensities. No attempt was made to adjust the RIR of annite in order to take its changing chemical composition into account for samples oxidized at various temperatures.

Mössbauer spectroscopy

A typical raw folded Mössbauer spectrum measured in the ±4 mm/s Doppler velocity range is shown in Figure 2a, for sample 350-5-W-k which contains comparable amounts of ferric and ferrous Fe. Here, the
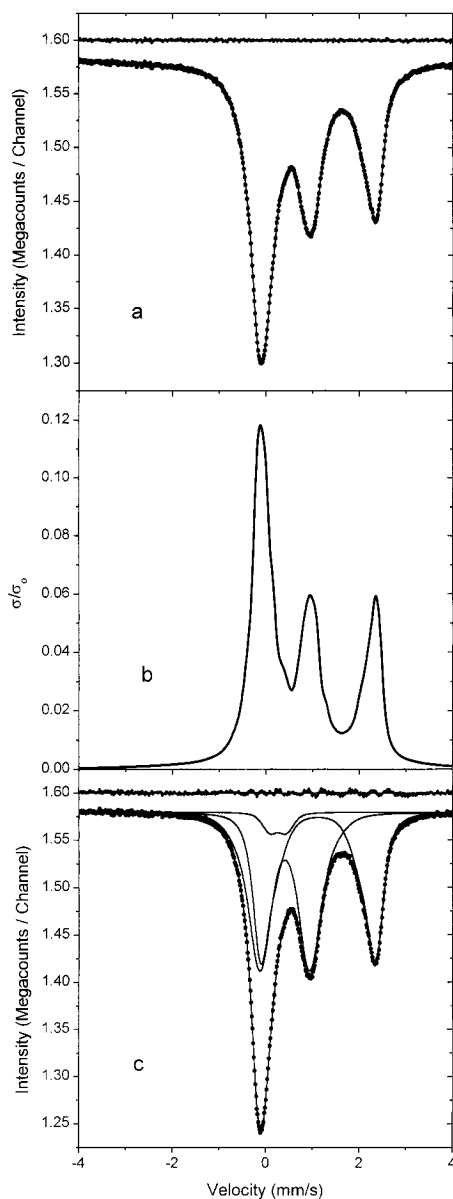
Figure 2. RT ^{57}Fe Mössbauer spectrum for sample 350-5-W-k, collected on the ±4 mm/s velocity range: (a) folded raw data with ideal Voigt-line fit and residual, used to extract the resonant absorber cross-section; (b) normalized resonant absorber cross-section extracted from the raw folded data; (c) QSD fit of the calculated thickness-corrected spectrum, showing the three doublets corresponding to the $^{[4]}Fe^{3+}$, $^{[6]}Fe^{3+}$ and $^{[6]}Fe^{2+}$ generalized sites, and the residual.

solid line represents the fitted theoretical curve, which is a sum of several Voigt lines (in this case, 22 lines) having independent Lorentzian widths, Gaussian widths, centers, and relative areas, that is used to extract the absorber resonant cross-section (Figure 2b) which, in turn, is used to generate the thickness-corrected transmission spectrum (Figure 2c), as explained above. The cross-section has narrower lines than the

thickness-corrected spectrum because, by definition, it does not contain broadening due to the source line-width. All spectra, in both the ±4 and ±11 mm/s velocity ranges, were thickness corrected in this way and final reported results are from fitting thickness-corrected spectra only.

The fit illustrated in Figure 2c is one where each of the assumed generalized sites, corresponding to $^{[4]}Fe^{3+}$, $^{[6]}Fe^{3+}$ and $^{[6]}Fe^{2+}$, is taken to have its own QSD. Each QSD is taken to be made up of a certain number of Gaussian components (Rancourt and Ping, 1991), where this number is only as large as can be justified on statistical grounds by the complexity of the spectral shape. For example, in the fit illustrated in Figure 2c, the $^{[4]}Fe^{3+}$ QSD is taken to have one Gaussian component, the $^{[6]}Fe^{3+}$ QSD is taken to have two Gaussian components, and the $^{[6]}Fe^{2+}$ QSD is also taken to have two Gaussian components. Such a fit is referred to as a 1-2-2 fit, with reference to the numbers of assumed Gaussian components in its $^{[4]}Fe^{3+}$, $^{[6]}Fe^{3+}$ and $^{[6]}Fe^{2+}$ sites, respectively. It is important to keep in mind that the individual Gaussian components, of a given QSD for a properly defined generalized site, have no independent physical or crystal chemical meaning. Only the actual corresponding QSDs can be interpreted (Rancourt, 1994a, 1994b; Rancourt et al., 1994c). As it turns out, as described below, the ±11 mm/s thickness-corrected spectrum (not shown) of sample 350-5-W-k shows that 2.7(2)% of the total spectral area is in a magnetically hyperfine split HFD component (or sextet), corresponding to an Fe oxide phase. This fact is neglected in the fit illustrated in Figure 2c. The corresponding fit parameters are given in Table 3, along with all the final fit parameters for the spectra measured on the ±4 mm/s velocity range, for all samples treated at temperatures up to 400°C.

Figure 3 shows the QSDs for the $^{[4]}Fe^{3+}$, $^{[6]}Fe^{3+}$ and $^{[6]}Fe^{2+}$ sites, respectively, corresponding to the fit of the spectrum for sample 350-5-W-k illustrated in Figure 2c and whose parameters are given in Table 3. Each curve is a continuous probability density (i.e. probability per unit of quadrupole splitting in mm/s) as a function of quadrupole splitting (QS) magnitude for all the QS magnitude values that are likely to occur in the particular generalized site (i.e. for the given cation in its particular tetrahedral or octahedral coordination). The spread in QS values occurs because of local chemical and structural disorder (e.g. Rancourt et al., 1994c; Rancourt, 1998). Each such QSD of QS magnitudes can be characterized by certain calculated parameters such as: the average QS, $\langle QS \rangle$, the standard deviation from the average, σ_{QSD}, and the QS of maximum probability density, QS_{peak}. Each generalized site is also characterized by an average CS, $\langle CS \rangle$, and a site population, expressed as a percentage of the total spectral area (or of total Fe, assuming equal recoilless fractions). These calculated characteristic parameters,
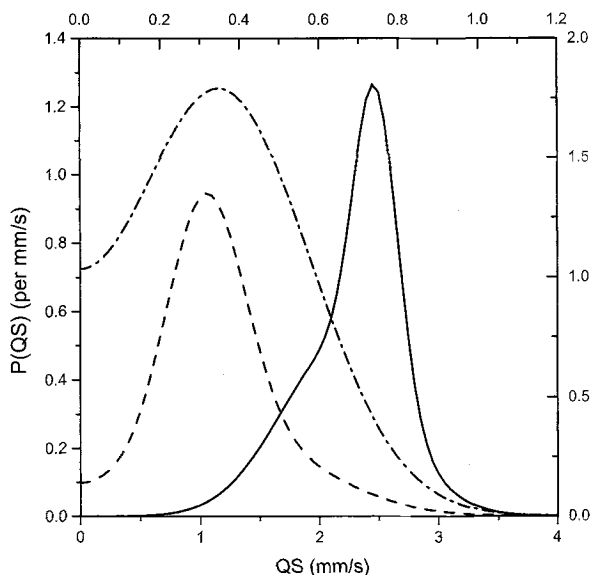
Figure 3.   QSDs corresponding to the fit illustrated in Figure 2c for: the $^{[4]}Fe^{3+}$ site (dash-dot line, upper and right scales); the $^{[6]}Fe^{3+}$ site (dashed line, lower and left scales); and the $^{[6]}Fe^{2+}$ site (solid line, lower and left scales).

corresponding to the fit parameters given in Table 3, are given in Table 4.

The spectra collected in a velocity range of ±11 mm/s showed no detectable magnetic hyperfine field split subspectra (*i.e.* no detectable sextet patterns that would be attributed to Fe oxide phases), to within the detection limit of ~0.2% of total Fe, for any of the samples heated to 250°C or lower. Also, there was no detectable ferrous Fe contribution in any of the spectra of any of the samples heated to 450°C or higher. Samples heated for 5 h at 300°C or higher all had detectable sextet patterns that were analyzed to quantify the amounts of Fe oxide phases. An example is given in Figure 4a where the ±11 mm/s RT raw folded spectrum for sample 500-5-W-m is shown with its Voigt-line fit (here 20 lines) used to generate the cross-section. The corresponding extracted absorber resonant cross-section is shown in Figure 4b. The calculated thickness-corrected spectrum is shown in Figure 4c, along with the fit that was used to quantify the sextet contribution. The latter fit is a 0-3-0-3 fit, with three assumed Gaussian components in the QSD of the paramagnetic Fe^{3+} doublet contribution and three assumed Gaussian components in the HFD of the magnetically ordered Fe^{3+} sextet contribution. We have excluded the small doublet contribution from $^{[4]}Fe^{3+}$ for simplicity. This does not affect the quantification of the sextet contribution or the characteristic features of the QSD of the dominant $^{[6]}Fe^{3+}$ doublet contribution. In order to account for this simplification, we allow the elemental doublet of the nominally $^{[6]}Fe^{3+}$ QSD to be asymmetric in intensity: $A_-/A_+ \neq 1$ (Rancourt and

Ping, 1991). Figure 4c (lower) illustrates the same fit as shown in Figure 4c (upper) on an expanded vertical scale, in order to show the sextet contribution better. The corresponding fit parameters are given in Table 5, along with those of the other ±11 mm/s RT thickness-corrected spectra, for all samples heated for 5 h at temperatures of 350°C or higher. The calculated Mössbauer parameters that characterize the generalized sites and their hyperfine parameter distributions are given in Table 6. Here $\langle\epsilon\rangle$ is the average value of ϵ, the usual perturbation-limit quadrupole shift of the sextet lines in an elemental sextet of the HFD (Rancourt and Ping, 1991). Table 6 also gives some raw site populations for the Fe oxide contribution obtained by fitting the raw uncorrected spectra. The latter are incorrect and are only given to illustrate the importance of performing thickness corrections. All hyperfine field parameters in both Tables 5 and 6 (z, σ_z, $\langle z\rangle$, σ_{HFD}, z_{peak}) and in this entire article are expressed in terms of the ^{57}Fe excited state Zeeman splitting, $z = g_N{}^*\sigma_N H$, in units of energy (*i.e.* Doppler velocity), rather than in units of magnetic field strength (Rancourt and Ping, 1991).

Elemental analyses (XRF, NRA, GC)

The XRF results, with accuracies calculated as explained above, can be stated as follows, with elemental amounts expressed as weight percentages of assumed oxides: 41.3(2)% Fe_2O_3, 30.2(3)% SiO_2, 8.6(1)% Al_2O_3, 14.55(1)% K_2O, and $-2(2)$% LOI (*i.e.* gain). The total is consistent with the known KCl impurity and the fact that Cl was not analyzed and the known ferric/ferrous ratio of the sample. Of all the usual elements, the only significant impurity was one of 1860(80) ppm of Co (0.2% Co), probably arising from an impurity in the starting materials. We expect Co to behave as Fe^{2+} in the annite structure. If we ignore the Co, the relevant elemental ratios and their accuracies can be expressed as: Al/Si = 0.337(5), Fe/Si = 1.03(1), and K/Si = 0.615(6), compared to the ideal values (expression 5) of ⅓, 1 and ⅓, respectively. The Al:Si:Fe ratio, therefore, is ideal within experimental error. At worst, there is a small excess of Fe (or Fe + Co), and no evidence for octahedral vacancies. The excess K is understood in terms of the synthesis method, as described above, and the excess (calculated as a weight ratio, KCl/annite = 12.3%) is in quantitative agreement with the amounts of KCl estimated by pXRD, that fall in the range KCl/annite = 6–19% (Table 2). These amounts of KCl are also consistent with the large (~10 μm) crystals of KCl that are seen in the SEM micrographs that have compositions confirmed by EDS (not shown).

The NRA results can be described as follows. If a given measurement is taken to be the average of several analyses on the plateau of H concentration values at a given spot and for a given beam energy, as explained above, then the 1σ statistical error in one such

measurement was $\sim 4 \times 10^{20}$ H/cm³. In taking the average of 17 such analyses, we obtain a final value of the intrinsic structural H concentration, in the starting annite, equal to $6.361(63) \times 10^{21}$ H/cm³, where the quoted error is the 1σ error in the mean. The latter error is comparable in magnitude to the estimated accuracy of 1–2%, arising from the uncertainty in dE/dx, as described above. The measured H concentration value can be compared to the calculated values, using the measured lattice parameters, for ideal annite, $KFe_3AlSi_3O_{10}(OH)_2$, annite in which the measured ferric Fe populations are taken to be caused by the oxybiotite reaction (expression 5), and annite in which the measured ferric Fe populations are taken to be caused by the vacancy mechanism (reaction 2). These calculated values are 7.811×10^{21}, 6.523×10^{21} and 7.811×10^{21} H/cm³, respectively. We find that the measured H concentration is equal to the value predicted by assuming that the oxybiotite reaction alone caused the measured ferric Fe populations, within experimental accuracy. This provides strong support that the oxybiotite reaction was the relevant reaction equilibrating Fe site populations in this hydrothermal synthesis and allows one to set an upper limit on octahedral vacancies in this sample, expressed as the ratio of vacancies to octahedral sites, □/Oct of $\sim 1\%$, compared to the known Fe^{3+}/Fe of $\sim 11\%$. By contrast, the vacancy mechanism prediction is ~ 20 standard deviations off the measured value.

The GC gives an independent evaluation of total H in the starting annite sample. The result based on 10 analyses is 0.33(1) wt.% H (one standard deviation error), in excellent agreement with the NRA result. This provides further strong support of the above conclusion regarding vacancies, as discussed below in relation to the relative quantification of H obtained by Raman spectroscopy (section on pillaring collapse transition). No S was detected. A small N signal is near the detection limit. There is also 0.122(1) wt.% C that probably substitutes for Si in the annite structure.

Raman spectroscopy

After much exploratory work over a wide frequency range, it was decided that two ranges were particularly useful: 200–1450 cm⁻¹ gave access to several bands that were not affected by the oxidation reactions studied and that could be used to provide integrated intensity calibrations, as explained above, and allowed a search for any Fe oxides or oxyhydroxides that would have formed (*e.g.* de Faria *et al.*, 1997), and 3500–3750 cm⁻¹ gave a detailed view of the relevant OH-stretching mode region. Figure 5 shows selected Raman spectra in the 200–1450 cm⁻¹ range, for the untreated annite and samples treated for 5 h at 250, 300, 350, 400, 500 and 600°C. The positions of the three bands (at 843, 896 and 1296 cm⁻¹) used for various nor-

malizations are shown by arrows. The two relatively broad bands that occur in the range 500–700 cm⁻¹ at $T_{TR} \geq 300°C$, with the more intense one centered at 560 cm⁻¹, are due to a poorly crystalline Fe oxide phase, as discussed below. A weak band occurring in the range 270–330 cm⁻¹ at $T_{TR} = 500–600°C$ is attributed to hematite and is also discussed in more detail below. These features correlate nicely with the observations of Fe oxides made by Mössbauer spectroscopy and pXRD (for hematite).

Selected normalized Raman spectra in the OH-stretching mode region are shown in Figure 6, where they are compared to the Fourier transform infrared (FTIR) transmission spectrum of the untreated annite sample discussed by Rancourt *et al.* (1994a). The deepest FTIR band at 3665 cm⁻¹ is unambiguously attributed to OH groups having their three adjacent nearest-neighbor octahedra occupied as $Fe^{2+}Fe^{2+}Fe^{2+}$ and is referred to as the normal (or N) band. The smaller bands at 3580 and 3545 cm⁻¹ were labeled I_a and I_b, respectively, by Rancourt *et al.* (1994a) who interpreted them as impurity (or I) bands. Based on the relative intensities of these three bands and on the fact that the I_b band increases in intensity (without significantly shifting its position) when the sample is partially oxidized, Rancourt *et al.* (1994a) suggested that I_a should be attributed to $Fe^{2+}Fe^{2+}Al^{3+}$ environments and that I_b should be attributed to $Fe^{2+}Fe^{2+}Fe^{3+}$ environments. This was in opposition to the interpretations of several authors who attributed weak bands at similar positions in natural biotite and synthetic annite (Redhammer *et al.*, 1993) samples as being due to OH groups that have nearest-neighbor octahedral cation vacancies. Such bands are called vacancy (or V) bands. Given the present work in which we establish an upper limit of □/Oct $\sim 1\%$ on the vacancy concentration in our untreated annite sample and in which we demonstrate that vacancies are not introduced into our heated samples until the oxybiotite reaction has mostly exhausted itself, there can now be no doubt that the I_a and I_b bands are not V bands. This therefore invalidates the key argument of Redhammer *et al.* (1993) that allowed them to conclude that the vacancy mechanism (reaction 2) was the main redox equilibrating mechanism in hydrothermal syntheses of annite. Redhammer *et al.* (2000) presented some evidence that their original (1993) IR band assignments were correct but this is based on annite-siderophyllite samples, in which, unlike with annite-oxyannite samples, trivalent octahedral cations (Al^{3+}) are not necessarily associated with loss of H. The very broad FTIR band centered at ~ 3450 cm⁻¹ and that is inferred to extend from ~ 3600 to ~ 3300 cm⁻¹ (Figure 6) is labeled W and is known to be due to sorbed water on both the annite powder and mostly the supporting KBr absorber material, since it can be reduced significantly in magnitude by drying treatments of either the KBr alone or the whole

Table 3. Mössbauer fitting parameters for $\pm$ 4 mm/s RT thickness corrected spectra[†].

Sample	BG (megacount/channel)	tof/nfp/χ^2_{red}	Site[‡]	δ_0 (mm/s)	δ_1	Area (counts, mm/s)	i	p_i (%)	Δ_i (mm/s)	$\sigma_{\Delta i}$ (mm/s)
ASIS–W-r	1.51201 (16)	1-1-3/20/2.61	A	0.259 (16)	0[*]	24,800 (2100)	1	100[*]	0.353 (23)	0.224 (23)
			B	0.446 (17)	0[*]	40,200 (2500)	1	100[*]	0.942 (42)	0.428 (27)
			C	1.1244 (46)	-0.0014 (17)	592,500 (1300)	1	45.9195[#]	2.6057 (24)	0.0946 (62)
							2	37.5 (6.4)	2.401 (32)	0.184 (13)
							3	16.57 (62)	2.266 (17)	0.732 (25)
ASIS–L-r	0.99668 (14)	1-1-3/20/1.13	A	0.20 (47)	0[*]	12,000 (10,000)	1	100[*]	0.51 (92)	0.46 (37)
			B	0.47 (52)	0[*]	11,000 (11,000)	1	100[*]	1.1 (1.1)	0.47 (28)
			C	1.161 (17)	-0.0158 (66)	196,400 (1,600)	1	26.2654[#]	2.5923 (80)	0.114 (14)
							2	44.3 (5.3)	2.441 (21)	0.254 (13)
							3	29.4 (1.9)	2.350 (36)	0.846 (55)
ASIS–S-r	2.71031 (21)	1-1-3/20/1.32	A	0.234 (30)	0[*]	16,200 (4700)	1	100[*]	0.335 (49)	0.260 (95)
			B	0.376 (21)	0[*]	28,700 (5100)	1	100[*]	0.996 (93)	0.396 (68)
			C	1.134 (18)	-0.0046 (67)	302,100 (1700)	1	44.737[#]	2.5951 (73)	0.095 (18)
							2	38 (18)	2.382 (89)	0.188 (38)
							3	16.9 (1.9)	2.206 (48)	0.683 (59)
250-5-W-m	2.35608 (16)	1-1-3/17/1.34	A	0.259[*]	0[*]	12,500 (1700)	1	100[*]	0.353[*]	0.224[*]
			B	0.375 (18)	0[*]	27,400 (2000)	1	100[*]	1.101 (51)	0.406 (46)
			C	1.1089 (96)	-0.0005 (37)	255,800 (1200)	1	80.1109[#]	2.541 (11)	0.1489 (72)
							2	13.0 (8.6)	2.179 (38)	0.103 (57)
							3	6.9 (8.4)	1.84 (46)	0.32 (23)
300-5-W-k	4.54966 (38)	1-2-3/23/2.95	A	0.237 (14)	0[*]	50,200 (5100)	1	100[*]	0.283 (13)	0.211 (23)
			B	0.4019 (34)	0[*]	358,800 (7200)	1	29.1559[#]	0 (260)	1.6 (2.9)
							2	70.8 (3.9)	1.0831 (78)	0.3639 (87)
			C	1.1218 (56)	$+0.0008$ (22)	1,139,900 (4000)	1	34.7323[#]	2.5954 (23)	0.1100 (62)
							2	33.8 (4.3)	2.362 (27)	0.219 (12)
							3	31.48 (63)	2.254 (11)	0.819 (20)
300-5-W-m	2.60232 (18)	1-1-3/17/1.59	A	0.259[*]	0[*]	17,100 (1500)	1	100[*]	0.353[*]	0.224[*]
			B	0.3828 (82)	0[*]	69,200 (1800)	1	100[*]	1.068 (20)	0.366 (16)
			C	1.052 (11)	$+0.0208$ (41)	246,600 (1500)	1	40.0523[#]	2.581 (20)	0.126 (44)
							2	46 (52)	2.38 (19)	0.207 (74)
							3	14.1 (9.5)	2.04 (28)	0.441 (97)
350-5-W-k	1.57943 (16)	1-2-2/17/2.14	A	0.259[*]	0[*]	19,900 (2200)	1	100[*]	0.353[*]	0.224[*]
			B	0.4057 (28)	0[*]	249,800 (2600)	1	39.7202[#]	1.301 (45)	0.734 (28)
							2	60.3 (3.2)	1.0464 (77)	0.3247 (74)
			C	1.109 (12)	$+0.043$ (52)	210,100 (1100)	1	40.2554[#]	2.4790 (44)	0.1830 (63)
							2	59.7 (1.6)	2.149 (17)	0.496 (10)
350-5-W-m	2.38582 (17)	1-1-2/15/2.01	A	0.259[*]	0[*]	14,500 (1600)	1	100[*]	0.353[*]	0.224[*]
			B	0.351 (15)	$+0.023$ (11)	142,000 (1800)	1	100[*]	1.0851 (95)	0.3751 (93)
			C	0.944 (24)	$+0.0661$ (89)	143,400 (1400)	1	65.7679[#]	2.451 (10)	0.196 (19)
							2	34 (15)	1.99 (18)	0.377 (84)
350-30-W-m	2.15104 (18)	1-1-3/17/1.20	A	0.259[*]	0[*]	13,700 (2000)	1	100[*]	0.353[*]	0.224[*]
			B	0.389 (19)	0[*]	32,800 (2800)	1	100[*]	1.074 (46)	0.402 (40)
			C	1.106 (11)	$+0.0061$ (41)	257,300 (2000)	1	47.0795[#]	2.546 (10)	0.131 (23)
							2	26 (23)	2.29 (20)	0.233 (81)
							3	26.9 (2.3)	2.269 (32)	0.909 (69)

https://doi.org/10.1346/CCMN.2001.0490601 Published online by Cambridge University Press

Table 3. Continued.

Sample	BG (megacount/channel)	tof/nfp/χ^2_{red}	Site‡	δ_0 (mm/s)	δ_1	Area (counts, mm/s)	i	p_i (%)	Δ_i (mm/s)	σ_{Δ_i} (mm/s)
350-5-S-k	2.34087 (19)	1-2-2/17/2.03	A	0.259*	0*	26,900 (1200)	1	100*	0.353*	0.224*
			B	0.3968 (26)	0*	290,500 (1400)	1	9.20869#	1.979 (76)	0.326 (54)
							2	90.8 (2.0)	1.081 (11)	0.3429 (77)
			C	1.087 (17)	+0.0149 (80)	176,500 (1300)	1	44.5325#	2.4377 (77)	0.203 (13)
							2	55.5 (5.2)	2.014 (47)	0.449 (20)
370-5-W-k	2.78070 (21)	1-2-2/17/4.59	A	0.259*	0*	42,300*	1	100*	0.353*	0.224*
			B	0.3365 (29)	+0.0955 (26)	729,300 (1800)	1	44.7579#	1.2530 (75)	0.885 (10)
							2	55.24 (56)	1.0371 (12)	0.2503 (18)
			C	1.140 (14)	−0.0279 (55)	289,900 (1600)	1	13.1764#	2.6199 (70)	0.092 (13)
							2	86.8 (10)	2.3575 (57)	0.4369 (62)
400-5-W-m	2.53569 (17)	1-3-1/20/1.16	A	0.189	0*	12,700 (3700)	1	100*	0.441 (29)	0.087 (55)
			B	0.389 (13)	−0.0061 (79)	276,100 (3900)	1	6.82504#	2.18 (17)	0.21 (12)
							2	30 (100)	1.01 (17)	0.27 (22)
							3	67 (91)	1.22 (38)	0.43 (18)
			C	1.048 (46)	0*	43,200 (1500)	1	100*	2.114 (89)	0.425 (25)

† BG is the flat background level of a folded-thickness-corrected spectrum; tof is the type-of-fit, as defined in the text; nfp is the number of free fitting parameters used; χ^2_{red} is the reduced χ^2 defined as χ^2 divided by the number of degrees of freedom. The Lorentzian full width at half maximum, Γ, is taken to have the natural linewidth value of 0.097 mm/s. All CS parameters are given with respect to the CS of metallic Fe at RT.

‡ A, B and C sites refer to $^{[4]}Fe^{3+}$, $^{[6]}Fe^{3+}$ and $^{[6]}Fe^{2+}$ generalized sites, respectively.

* This parameter frozen during fit.

This parameter constrained by a normalized condition: sum of all population probabilities must be 100%.

Table 4. Calculated Mössbauer parameter for ±4 mm/s RT thickness corrected spectra.

Sample	Site[1]	$\langle CS \rangle$ (mm/s)	$\langle QS \rangle$ (mm/s)	σ_{QSD} (mm/s)	QS_{peak} (mm/s)	Site population (%)
ASIS-W-r	A	0.259	0.364	0.206	0.347	3.78 (31)
	B	0.446	0.946	0.418	0.942	6.11 (35)
	C	1.128	2.473	0.350	2.593	90.12 (44)
ASIS-L-r	A	0.200	0.574	0.381	0.350	5.6 (4.5)
	B	0.472	1.091	0.463	1.088	5.1 (4.8)
	C	1.123	2.454	0.498	2.574	89.3 (6.2)
ASIS-S-r	A	0.234	0.359	0.225	0.303	4.7 (1.3)
	B	0.376	0.997	0.392	0.996	8.3 (1.3)
	C	1.123	2.448	0.343	2.582	87.1 (1.7)
250-5-W-m	A	0.259^2	0.364^2	0.206^2	0.347^2	4.22 (56)
	B	0.375	1.102	0.403	1.101	9.28 (63)
	C	1.108	2.446	0.260	2.540	86.50 (78)
300-5-W-k	A	0.237	0.301	0.185	0.264	3.24 (32)
	B	0.402	1.141	0.611	1.075	23.16 (37)
	C	1.124	2.409	0.500	2.578	73.59 (43)
300-5-W-m	A	0.259^2	0.364^2	0.206^2	0.347^2	5.15 (44)
	B	0.383	1.068	0.365	1.068	20.78 (44)
	C	1.102	2.413	0.291	2.546	74.07 (53)
350-5-W-k	A	0.259^2	0.364^2	0.206^2	0.347^2	4.14 (44)
	B	0.406	1.156	0.522	1.059	52.08 (38)
	C	1.119	2.282	0.432	2.460	43.78 (34)
350-5-W-m	A	0.259^2	0.364^2	0.206^2	0.347^2	4.85 (50)
	B	0.376	1.086	0.374	1.085	47.35 (45)
	C	1.096	2.295	0.347	2.435	47.80 (45)
350-30-W-m	A	0.259^2	0.364^2	0.206^2	0.347^2	4.52 (64)
	B	0.389	1.075	0.399	1.074	10.79 (83)
	C	1.121	2.407	0.508	2.532	84.69 (97)
350-5-S-k	A	0.259^2	0.364^2	0.206^2	0.347^2	5.44 (24)
	B	0.397	1.164	0.429	1.083	58.82 (24)
	C	1.120	2.202	0.418	2.406	35.73 (22)
370-5-W-k	A	0.259^2	0.364^2	0.206^2	0.347^2	3.98^2
	B	0.445	1.162	0.577	1.039	68.70 (11)
	C	1.073	2.392	0.418	2.607	27.31 (12)
400-5-W-m	A	0.189	0.441	0.087	0.441	3.8 (1.1)
	B	0.382	1.234	0.466	1.097	83.2 (1.0)
	C	1.048	2.114	0.425	2.113	13.02 (45)

[1] *A*, *B* and *C* sites refer to $^{[4]}Fe^{3+}$, $^{[6]}Fe^{3+}$ and $^{[6]}Fe^{2+}$ generalized sites, respectively.

[2] This parameter constrained by a fitting parameter that was frozen during fit.

absorber pressed pellets. The Raman spectra (Figure 6) and other spectra measured over larger wavenumber ranges (not shown) show that only the N band seems to be Raman active. This is probably not due to a strict selection rule arising from symmetry but more likely due to significant differences in intrinsic Raman intensities for the N, I and W bands. Such large differences between Raman and FTIR of the intrinsic intensities of different OH-group stretching bands are common in layer silicates (*e.g.* Pajcini and Dhamelincourt, 1994; Robert *et al.,* 1989). It is also known that sorbed water is less Raman intense than structural OH bands, although intercalated water is easily measured in, for example, vermiculite (Wada and Kamitakahara, 1991). The intrinsic Raman preference for the N band that we observe may be a consequence of the fact that only the N band OH groups are aligned close to the *c* axis, in that Raman intensity depends on OH electric dipole moment to lattice vibration coupling, and lattice vibrations along *c* may be particularly easily induced by

radiation-driven oscillations of *c*-aligned OH groups, relative to I band OH groups that are not aligned to specific crystallographic directions and that tend to lie closer to the stiffer *ab* plane. In any case, our comparison (Figure 6) shows that all but the N band are effectively forbidden. This provides us with the opportunity to follow directly the population of N band OH groups as oxidation proceeds, a feature that we use below.

DISCUSSION AND FURTHER RESULTS

Crystal chemical nature of the oxidation

General observations. The first observation is that, on heating the synthetic annite sample up to 600°C, the crystal structure stays intact, with only small changes in lattice parameters and only small amounts of ancillary phases being produced (Tables 1 and 2; Figure 1). The heated material remains a mica that is similar to the original annite. This is consistent with all previous
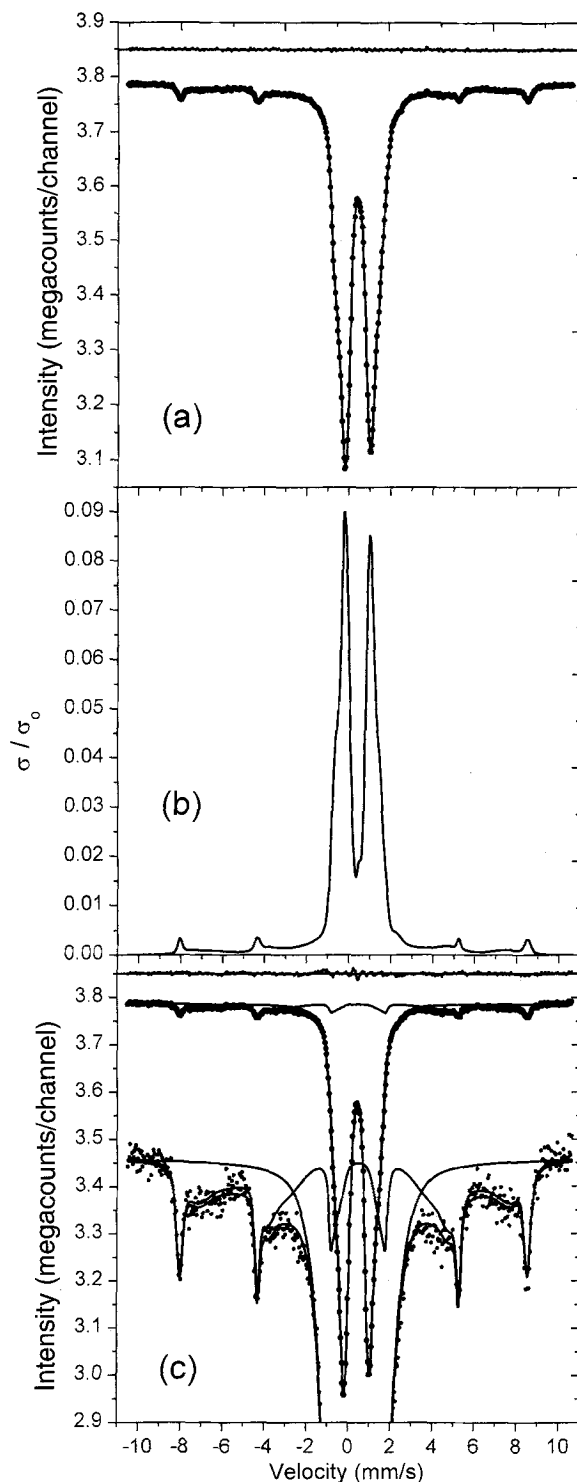
Figure 4. RT ^{57}Fe Mössbauer spectrum for sample 500-5-W-m, collected on the ± 11 mm/s velocity range: (a) folded raw data with ideal Voigt-line fit and residual, used to extract the resonant absorber cross-section; (b) normalized resonant absorber cross-section extracted from the raw folded data; and (c) QSD+HFD fit of the calculated thickness corrected spectrum, showing the two assumed contributions, a QSD doublet that models the intra-mica Fe^{3+} and a HFD sextet that models

studies where biotite samples were heated in air (e.g. Farmer et al., 1971; Ferrow, 1987; Güttler et al., 1989; Hogg and Meads, 1975; Ivanitskiy et al., 1975; Rancourt et al., 1993a; Rimsaite, 1970; Robert, 1971; Sanz et al., 1983; Tricker et al., 1976; Vedder and Wilkins, 1969).

The second main feature is that all of the structural $^{[6]}$Fe^{2+} is oxidized to $^{[6]}$Fe^{3+} when the sample is heated for 5 h at 450°C or above (Tables 4 and 6). The latter temperature of complete oxidation, for a 5 h exposure, is significantly lower than that found in natural biotite samples heated for comparable durations (e.g. Farmer et al., 1971; Güttler et al., 1989; Hellner and Euler, 1957; Hogg and Meads, 1975; Ivanitskiy et al., 1975; Rancourt et al., 1993a; Robert, 1971; Sanz et al., 1983; Vedder and Wilkins, 1969). This difference can be attributed to two special characteristics of our sample: its large Fe content and its small particle size. We now show how the changes in lattice parameters and the appearance of ancillary phases are linked directly to the degree of oxidation.

Figure 7 shows the site populations of $^{[6]}$Fe^{2+} and $^{[6]}$Fe^{3+} in heated annite, obtained by Mössbauer spectroscopy as percentages of total Fe, as functions of the treatment temperature, T_{TR}, for 5 h treatments. Figures 8a–d show the lattice parameters a, b, c, and the cell volume, v_{cell}, respectively, as functions of the treatment temperature. The values for the original starting synthetic annite sample are also shown. On first examination, the dependence of $^{[6]}$Fe^{2+}/Fe on T_{TR} is closely mimicked by the dependencies of the lattice parameters on T_{TR}. Although there are important differences in these dependencies, which are discussed below, the overall degree of correlation between $^{[6]}$Fe^{2+}/Fe and the lattice parameters (Figures 7 and 8) is high and clearly suggests that the amount of oxidation is a key controlling factor of the lattice parameters. For treatment temperatures of 450°C and above (5 h exposures), where the Fe oxidation is complete, the lattice parameters are constant, as are the amounts of ancillary phases and the Mössbauer parameters (see below). The high-temperature oxidized phase (ferrioxyannite) is refractory to further change and stable to at least 600°C.

In examining Figure 7, one notes a gradual monotonic variation in the degree of oxidation with T_{TR}. There is no evidence, such as a plateau separating two sloped regions, that more than one oxidation mechanism or reaction occurs. In addition, there is no change in behavior, such as a change in slope or a discontinuity or a plateau, at the magic $^{[6]}$Fe^{2+}/Fe ratio value of ⅓ that would suggest that the oxybiotite reaction

←

the Fe oxide phases. An expanded view of the latter fit is also shown in Figure 4c, showing the sextet in more detail.

Rancourt *et al.*

Clays and Clay Minerals

Table 5. Mössbauer fitting parameters for ±11 mm/s RT thickness corrected spectra.[†]

Sample	BG (mega-counts/channel)	tof/nfp/χ^2_{red}	Site	δ_0 (mm/s)	δ_1	ϵ_0 (mm/s)	Area (counts, mm/s)	A_-/A_+ or A_2/A_3	i	p_i (%)	Δ_i or z_i (mm/s)	$\sigma_{\Delta i}$ or σ_{zi} (mm/s)
350-5-W-k	7.0466*	0-2-2-2/22/2.99	B	0.4318 (72)	+0.0201 (67)	—	1,236,100 (5300)	1.0709 (47)	1	51.274#	1.055 (15)	0.981 (27)
									2	48.7 (1.4)	1.0039 (36)	0.2989 (51)
			C	1.119 (18)	−0.0034 (68)	—	881,000 (5000)	1*	1	32.4353#	2.5941 (49)	0.1635 (70)
									2	67.6 (1.6)	2.308 (12)	0.4527 (75)
			D	0.504 (99)	0*	−0.110*	58,700 (4800)	2*	1	6.53436*	3.458 (63)	0.044 (87)
									2	93.5 (4.5)	2.6*	0.6*
370-5-W-k	4.77358*	0-2-2-2/24/3.97	B	0.4254 (26)	+0.0152 (26)	—	1,672,400 (3600)	1.0825	1	48.9276#	1.209 (13)	0.748 (10)
									2	51.1 (1.4)	1.0221 (18)	0.2932 (37)
			C	1.234 (21)	−0.0524 (76)	—	755,500 (3300)	1*	1	25.9659#	2.6381 (63)	0.1722 (92)
									2	74.0 (1.7)	2.185 (17)	0.4650 (94)
			D	0.391 (18)	0*	−0.110 (18)	75,500 (4100)	3.26 (44)	1	16.879#	3.4693 (95)	0.010 (31)
									2	83.1 (2.5)	2.6*	0.6*
400-5-W-m	4.24602*	0-3-2-2/28/4.71	B	0.4389 (26)	−0.0010 (21)	—	1,290,300 (4000)	1.0212 (22)	1	21.8051#	1.215 (57)	0.211 (32)
									2	68.5 (1.1)	1.3129 (47)	0.6985 (92)
									3	9.7 (5.2)	0.878 (45)	0.142 (27)
			C	1.1281 (39)	0*	—	210,600 (3600)	1*	1	84.3073#	2.339 (25)	0.497 (13)
									2	15.72 (2.1)	1.9606 (93)	0.0 (6.1)
			D	0.540 (62)	0*	−0.058 (53)	115,900 (5100)	2.45 (31)	1	17 (12)	3.423 (50)	0.202 (85)
									2	82.9031#	2.59 (14)	0.60 (12)
450-5-W-m	4.272*	0-3-0-3/23/2.25	B	0.4291 (19)	−0.0083 (17)	—	1,226,200 (4200)	1.0944 (24)	1	55.0861#	1.1643 (58)	0.3179 (49)
									2	20.4 (11)	2.004 (18)	0.338 (13)
									3	24.50 (53)	−1.01 (20)	1.74 (15)
			D	0.340 (15)	0*	−0.138 (15)	153,700 (5900)	2.11 (17)	1	11.8543#	3.5094 (94)	0.035 (18)
									2	19.0 (7.5)	3.229 (71)	0.206 (68)
									3	69.1 (5.8)	2.6*	0.592 (86)
500-5-W-m	3.7865*	0-3-0-3/23/2.52	B	0.4175 (15)	−0.0053 (12)	—	1,407,700 (4100)	1.0786 (19)	1	23.2082#	2.035 (11)	0.3389 (85)
									2	56.79 (75)	1.1665 (37)	0.3133 (34)
									3	20.00 (41)	−0.86 (37)	1.84 (21)
			D	0.3621 (76)	0*	−0.1102 (76)	166,800 (5600)	2.35 (13)	1	24.7437#	3.4836 (47)	0.0437 (87)
									2	20.4 (7.0)	3.165 (69)	0.230 (67)
									3	54.8 (5.5)	2.6*	0.592 (94)
550-5-W-m	4.588*	0-3-0-3/23/2.61	B	0.4156 (17)	−0.0050 (14)	—	1,319,800 (4100)	1.0705 (22)	1	25.0818#	2.039 (11)	0.3464 (89)
									2	57.88 (80)	1.1620 (37)	0.3023 (35)
									3	17.03 (48)	−0.71 (72)	1.89 (31)
			D	0.3627 (65)	0*	−0.1151 (65)	174,000 (5900)	2.24 (12)	1	27.0806#	3.4804 (38)	0.0345 (69)
									2	17.5 (5.5)	3.128 (60)	0.218 (70)
									3	55.4 (4.7)	2.6*	0.625 (95)
600-5-W-m	4.244*	0-3-0-3/23/2.49	B	0.4142 (17)	−0.0042 (15)	—	1,291,400 (3700)	1.0689 (24)	1	24.8487#	2.048 (11)	0.3444 (86)
									2	57.42 (74)	1.1646 (35)	0.2997 (33)
									3	17.73 (47)	−0.67 (73)	1.84 (30)
			D	0.3606 (48)	0*	−0.1096 (48)	174,500 (5600)	2.19 (10)	1	32.0273#	3.4676 (27)	0.0272 (54)

Table 5. Continued.

Sample	BG (mega-counts/ channel)	tof/nfp/χ^2_{red}	Site	δ_0 (mm/s)	ϵ_0 (mm/s)	δ_i	Area (counts, mm/s)	A_1/A_3 or A_2/A_3	i	p_i (%)	Δ_i or z_i (mm/s)	σ_{ai} or σ_{3i} (mm/s)
									2	13.5 (4.3)	3.178 (56)	0.173 (63)
									3	54.5 (37)	2.6*	0.644 (88)

† BG is the flat background level of a folded thickness corrected spectrum; tof is the type-of-fit, as defined in the text; nfp is the number of free fitting parameters used; χ^2_{red} is the reduced χ^2, defined as χ^2 divided by the number of degrees of freedom. The Lorentzian full width at half maximum, Γ, is taken to have the natural linewidth value of 0.097 mm/s. All CS parameters are given with respect to the CS of metallic iron at RT.

‡ B, C and D sites refer to $^{[6]}Fe^{3+}$, $^{[6]}Fe^{2+}$ and Fe oxide generalized sites, respectively. The $^{[4]}Fe^{3+}$ site is not modeled and should be considered to be part of the effective $^{[6]}Fe^{3+}$ site.

* This parameter frozen during fit.

This parameter constrained by a normalization condition: sum of all population probabilities must be 100%.

(reaction 1) is the dominant reaction. The ⅓ value is the value that would correspond exactly to the exhaustion of all structural OH groups, via reaction 1, assuming there are no vacancies in the starting annite material. Taken alone, Figure 7 seems to suggest that a single oxidation reaction is acting and that it is not the oxybiotite reaction. The logic leading to these conclusions, however, is not rigorous. At most, Figure 7 demonstrates that reaction 1 cannot be the only reaction acting. Further examination shows that several discontinuities in other properties occur at the $^{[6]}Fe^{2+}/$ Fe ratio value of ⅓ which suggest that reaction 1 is the dominant reaction at the lower temperatures, up to its completion where the OH groups have been totally depleted.

Pillaring collapse transition at point of total OH loss. The most striking of these discontinuities in behavior is the discontinuity in c itself that occurs between $T_{TR} =$ 350 and 370°C, precisely where the $^{[6]}Fe^{2+}/Fe$ ratio value of ⅓ is crossed (Figures 7 and 8c). We interpret this abrupt change as a pillaring collapse transition that occurs near the point where the OH concentration becomes zero as oxidation proceeds. Takeda and Ross (1975) observed a difference in c of similar magnitude (0.09 Å compared to our ~0.11 Å) between a natural oxybiotite and its synthetically hydrogenated counterpart. The gradual pre-transition decrease in c (Figure 8c) can be tentatively interpreted as progressive OH axis bending away from the c axis, as more and more of the electrostatic interlayer compressional force is countered by fewer and fewer OH groups (whose protons oppose the K^+ interlayer cations). Such bending is consistent with the fact that, as the annite is oxidized, a larger and larger fraction of the remaining OH groups see $^{[6]}Fe^{2+}$-$^{[6]}Fe^{2+}$-$^{[6]}Fe^{3+}$ or $^{[6]}Fe^{2+}$-$^{[6]}Fe^{3+}$-$^{[6]}Fe^{3+}$ nearest-neighbor configurations, rather than the dominant $^{[6]}Fe^{2+}$-$^{[6]}Fe^{2+}$-$^{[6]}Fe^{2+}$ nearest-neighbor configuration of unoxidized annite (Gilkes *et al.*, 1972a, 1972b).

These interpretations are consistent with the crystal chemical idea that, for a fixed tetrahedral-site stoichiometry, the c axis is predominantly sensitive to the nature of the OH site anion, rather than being determined by the octahedral site cationic species (Ferrow and Annersten, 1984; Ferrow, 1987, 1990; Hazen and Wones, 1972; Ohta *et al.,* 1982), such as is the case for the a and b parameters. This is illustrated in Figure 9 where c is plotted *vs.* a for: the original and oxidized annite samples of the present study; two synthetic Fe-Mg (annite-phlogopite) solid-solutions (Mercier, 2001); a synthetic Fe-Ni (annite-Ni-end-member) solid-solution (Redhammer, 1998; Mercier, 2001); and a synthetic OH-F (annite-fluorannite) series (Rancourt *et al.,* 1996; Mercier, 2001). We see that, although a varies as expected with average octahedral cation radius (as does b, by virtue of the re-

Table 6. Calculated Mössbauer parameters for ± 11 mm/s RT thickness corrected spectra.

Sample	Site[1]	$\langle CS \rangle$ (mm/s)	$\langle QS \rangle$ or $\langle z \rangle$ (mm/s)	σ_{QSD} or σ_{HFD} (mm/s)	QS_{peak} or z_{peak} (mm/s)	$\langle \epsilon \rangle$ (mm/s)	Site pop. (cor.) (%)	Site pop. (raw) (%)
350-5-W-k	B	0.452	1.102	0.619	0.999	—	56.81 (21)	—
	C	1.111	2.401	0.406	2.572	—	40.49 (19)	—
	D	0.504	2.656	0.618	3.456	−0.110	2.70 (21)	—
370-5-W-d	B	0.442	1.130	0.538	1.031	—	66.80 (15)	—
	C	1.113	2.302	0.455	2.597	—	30.18 (11)	—
	D	0.391	2.747	0.637	2.469	−0.110	3.02 (16)	—
400-5-W-m	B	0.438	1.261	0.578	1.180	—	79.80 (31)	—
	C	1.128	2.280	0.477	1.973	—	13.03 (20)	—
	D	0.540	2.731	0.637	3.357	−0.058	7.17 (29)	—
450-5-W-m	B	0.422	1.446	0.738	1.174	—	88.86 (38)	86.60 (42)
	D	0.340	2.827	0.610	3.508	−0.138	11.14 (38)	13.40 (42)
500-5-W-m	B	0.412	1.460	0.714	1.175	—	89.40 (32)	87.16 (35)
	D	0.362	2.934	0.592	3.483	−0.110	10.60 (32)	12.84 (35)
500-5-W-m	B	0.410	1.458	0.687	1.170	—	88.35 (35)	86.32 (39)
	D	0.363	2.931	0.612	3.480	−0.115	11.65 (35)	13.68 (39)
600-5-W-m	B	0.410	1.455	0.682	1.172	—	88.09 (34)	86.04 (37)
	D	0.361	2.956	0.624	3.467	−0.110	11.91 (34)	13.96 (37)

[1] *B, C* and *D* sites refer to $^{[6]}Fe^{3+}$, $^{[6]}Fe^{2+}$ and Fe oxide generalized sites, respectively. The $^{[4]}Fe^{3+}$ site is not modeled and should be considered to be part of the effective $^{[6]}Fe^{3+}$ site.
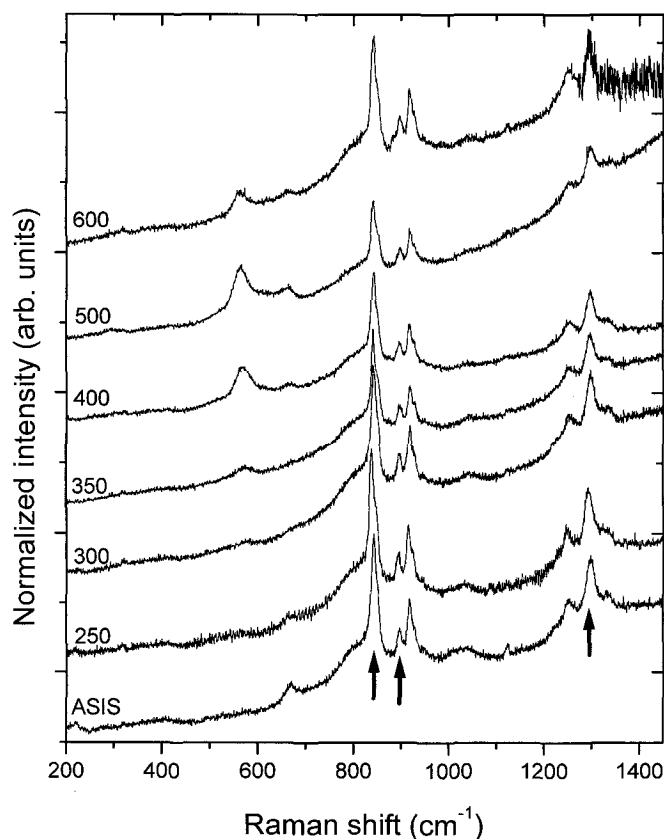
Figure 5. Typical Raman spectra in the range 200–1450 cm^{-1}, for the untreated annite sample (ASIS) and for samples treated for 5 h at various temperatures (°C), as indicated. The arrows show the positions of three peaks used to normalize the OH peak at 3660 cm^{-1}. Each spectrum was normalized by dividing by its largest value, in order to establish a convenient scale for the figure, and each spectrum is shifted vertically by a set amount for clarity.
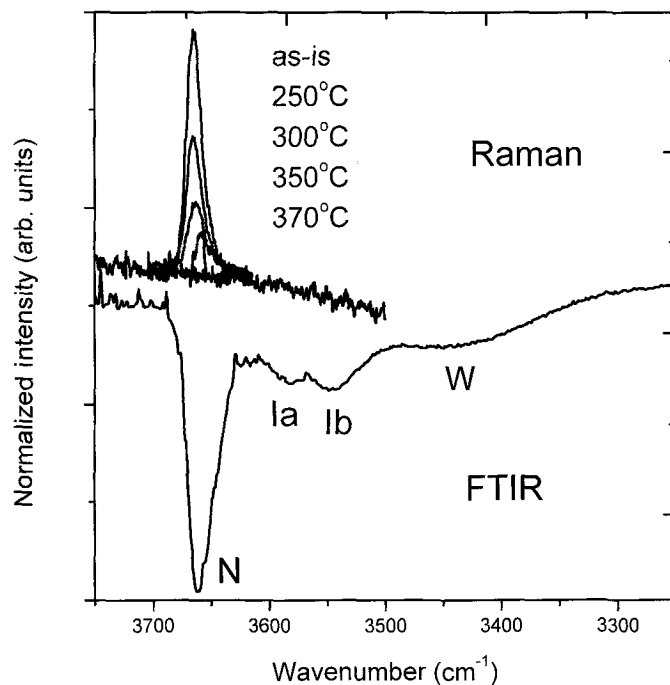
Figure 6. Raman spectra in the OH-stretching range 3500–3750 cm^{-1} for the untreated annite sample and for samples treated for 5 h at 250, 300, 350 and 370°C, in sequence of decreasing peak intensity, as indicated, compared to the FTIR transmission spectrum of the untreated annite sample (Rancourt *et al.,* 1994a). The transmission in the FTIR spectrum is on a linear scale and spans the range 78.5 to 86.5%. The N, I_a and I_b bands are indicated, following Rancourt *et al.* (1994a). Only an N band is detected by Raman spectroscopy. The broad band due to sorbed water from the KBr absorber material used in the FTIR measurement is indicated as W.
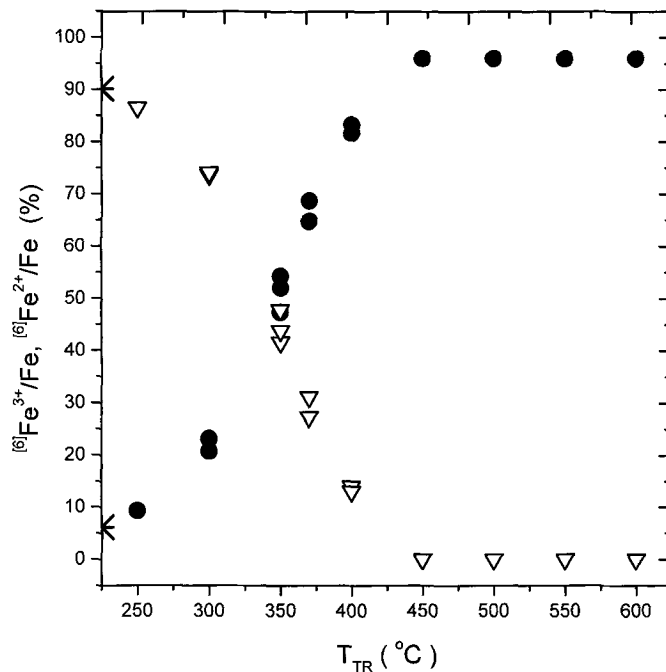
Figure 7. [6]Fe^{3+} (filled circles) and [6]Fe^{2+} (open triangles) populations, expressed as fractions of total intra-mica Fe in %, as functions of the treatment temperature for 5 h treatments. The results for the starting unoxidized annite sample are shown (stars) on the left axis.
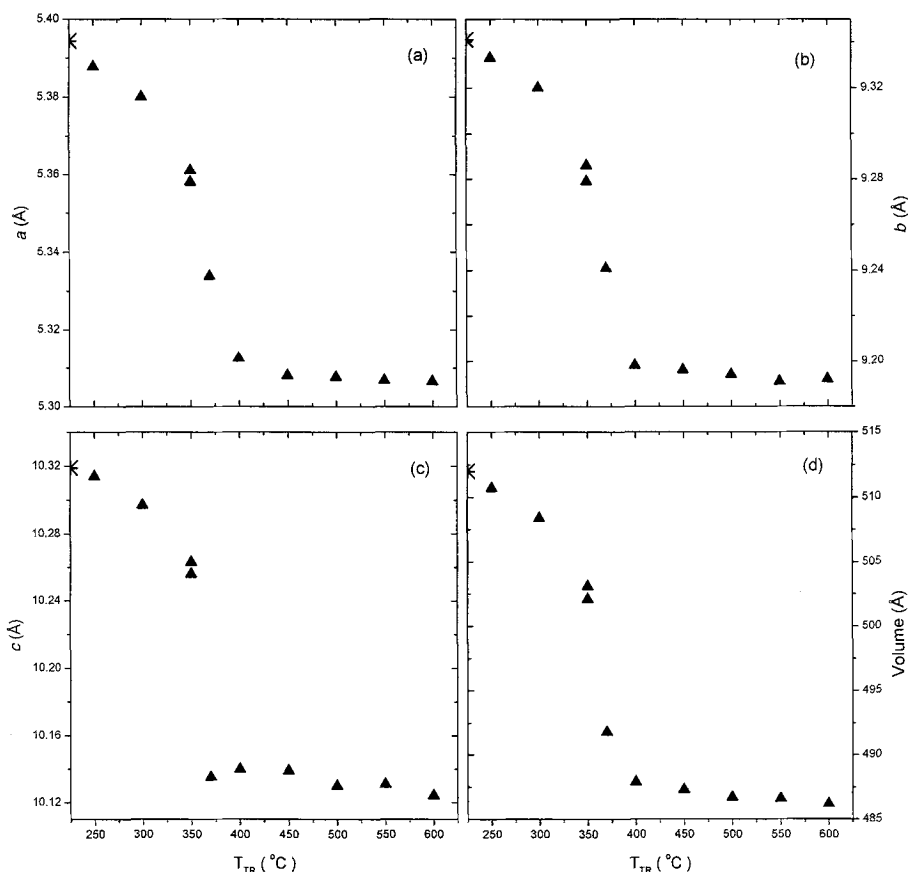
Figure 8.   Lattice parameters for the starting unoxidized annite sample and for the oxidized annite samples shown as functions of the treatment temperature for 5 h treatments: (a) *a*; (b) *b*; (c) *c*; and (d) cell volume. The values for the starting unoxidized annite sample are shown (stars) on the left axes.

lationship illustrated in Figure 1), *c* is relatively constant for all series that has saturation amounts of structural OH (synthetic Fe-Mg and Fe-Ni) and only has lower values when structural H is removed, either via OH loss (*i.e.* OH^-/O^{2-} substitution) or via OH/F substitution. It is noted that, once all OH groups have been lost in our oxidized annite samples ($T_{TR} \geq 370°C$), the *c* value is again constant, despite continued oxidation on further heating and associated changes in *a*. Figure 9, therefore, gives strong evidence that our interpretation of Figure 8c, in terms of a pillaring collapse transition preceded by OH-bending away from the *c* axis, is correct.

This interpretation is further supported by our H analyses, that are illustrated in Figure 10. This figure shows ratios of H contents (left scale) *vs.* the treatment temperature. The results are also given on an absolute wt.% H scale (right scale) that is valid within the approximation that the sample weight does not change significantly as the sample is heated at these treatment temperatures. The filled squares represent total H relative to total H in the starting annite (H_{total}/H_{as-is}) calculated from the ferric Fe populations measured using

Mössbauer spectroscopy by assuming that the oxybiotite reaction acts alone. The filled diamonds represent the H present in the normal (N) contribution measured by Raman spectroscopy relative to the same (N) contribution measured by Raman spectroscopy in the starting annite (H_N/H_{as-is}). The open diamonds are calculated values of H_N/H_{as-is}, for comparison with the measured Raman values, obtained by using the measured ferric and ferrous amounts from Mössbauer spectroscopy and assuming random cation and OH distributions and no vacancies. The important point here is that the H detected by Raman spectroscopy (H_N/H_{as-is}) drops to a value of zero (undetected) between $T_{TR} = 350$ and $370°C$, at the same treatment temperatures between which the bridging collapse transition occurs (Figure 8c). This corroborates our interpretation of the bridging collapse transition and gives strong support to all our observations that are consistent with the oxybiotite reaction proceeding first to exhaust all H before the vacancy reaction becomes the main oxidizing reaction, as the sample is treated at increasing temperatures. The total-H curve (H_{total}/H_{as-is}) is above the H_N/H_{as-is} curves, as expected from
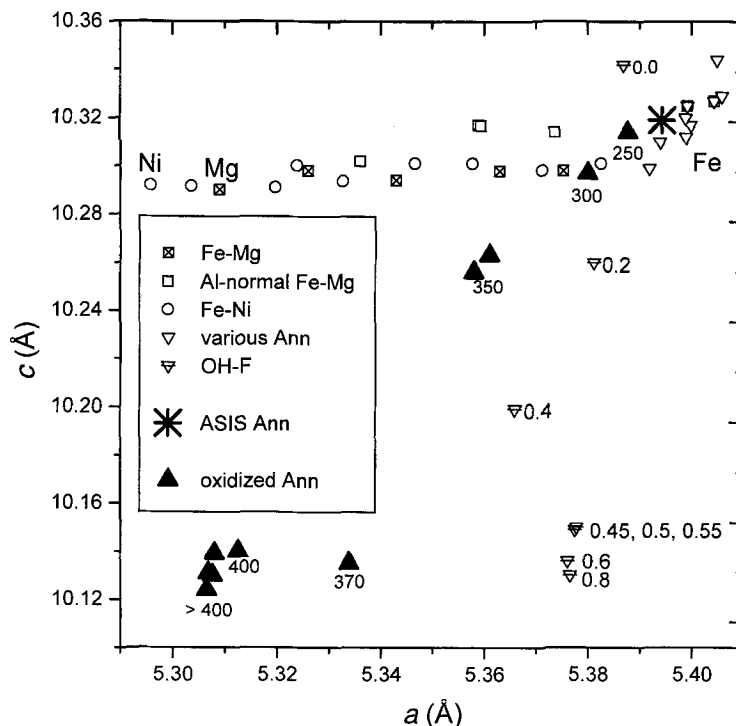
Figure 9. *c vs. a* for the starting unoxidized annite sample and for the oxidized annite samples (treated for 5 h at the temperatures indicated (°C)) compared to the values for other synthetic mica samples: two Fe-Mg series, an Fe-Ni series, various synthetic annite samples, and an annite-fluorannite series where the nominal F/(F+OH) ratio is indicated (Mercier, 2001). The approximate positions of the Ni, Mg (phlogopite), and Fe (annite) end-members are indicated by Ni, Mg and Fe, respectively.

the fact that oxidation produces $^{[6]}Fe^{3+}$ thereby reducing the number of N-type environments for OH groups. The H_N/H_{as-is} measured by Raman is above the calculated H_N/H_{as-is} at 350°C and below the calculated values at 250 and 300°C. This can be understood in terms of strong correlations between OH and $^{[6]}Fe^{3+}$, that are consistent with the oxybiotite reaction. For example, the remaining OH groups at small OH concentrations can be expected to be associated with Fe^{2+}-Fe^{2+}-Fe^{2+} environments where the oxybiotite reaction has not yet acted locally whereas the OH groups at intermediate OH concentrations are expected to be preferentially associated with Fe^{2+}-Fe^{2+}-Fe^{3+} environments because the latter environments become more abundant as oxidation proceeds, until too much of the H itself is removed by further oxidation.

The inset of Figure 10 compares three values of H content (right scale) for the untreated annite: (1) the calculated value (MS) obtained from the measured Mössbauer ferric/ferrous ratio by assuming that the starting annite contains no vacancies and that its ferric fraction has been caused by the oxybiotite reaction acting alone; (2) the measured result from NRA described above, calculated as a weight percent by using the calculated density from the lattice parameters; and (3) the measured value from GC. These three values

(0.329(7), 0.321(3), and 0.33(1) wt.% H, respectively) are in excellent agreement and can be compared to the calculated values, using the same measured lattice parameters, for ideal annite (0.394 wt.% H) and for annite in which the measured ferric Fe populations are assumed to be caused by the vacancy mechanism alone (0.399 wt.% H). The reported errors are one standard deviation error and the error in the Mössbauer (MS, Figure 10 inset) evaluation is from the error in the ferric Fe-site populations alone. In combination with the other measurements presented above (XRF, NRA), there can be little doubt that the ferric Fe in our starting annite has arisen predominantly from the oxybiotite reaction and that this sample does not contain vacancies ($\square$/Oct <1%).

Next, we present several lines of evidence that show the vacancy mechanism (reaction 2) to be mostly inoperative until a complete depletion of OH has occurred (by the oxybiotite reaction) and to be the predominant oxidation mechanism in the absence of OH groups and up to complete oxidation of the remaining ferrous Fe. This evidence includes: TGA and DTA signals of both the absence and presence of Fe-oxide formation; direct quantification of Fe-oxide formation by Mössbauer spectroscopy; pXRD and Raman spectroscopy; local-environment characterization based on Mössbauer
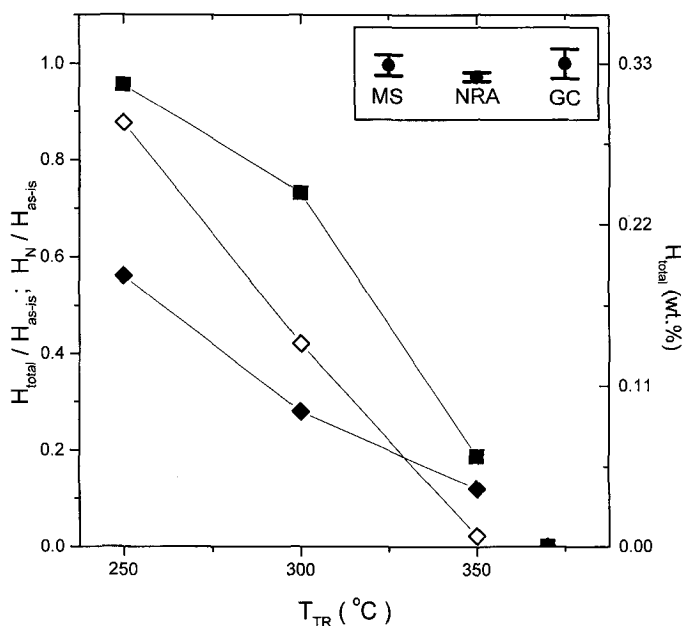
Figure 10. Measured and calculated ratios of H contents (left scale) *vs.* the treatment temperature. The results are also given on an absolute wt.% H scale (right scale) that is valid within the approximation that the sample weight does not change significantly as the sample is heated at these treatment temperatures. Filled squares represent total H relative to total H in the starting annite (H_{total}/H_{as-is}) calculated from the ferric Fe populations measured by Mössbauer spectroscopy by assuming that the oxybiotite reaction acts alone. Filled diamonds represent the H present in the normal (N) contribution measured by Raman spectroscopy relative to the same (N) contribution measured by Raman spectroscopy in the starting annite (H_N/H_{as-is}). Open diamonds represent calculated values of H_N/H_{as-is} obtained by using the measured ferric and ferrous amounts from Mössbauer spectroscopy and assuming random cation and OH distributions and no vacancies. The inset shows three values of H content (right scale) for the untreated annite: (1) the calculated value (MS) obtained from the measured Mössbauer ferric/ferrous ratio by assuming that the starting annite contains no vacancies and that its ferric fraction has been caused by the oxybiotite reaction acting alone; (2) the measured result from NRA, calculated as a wt.% by using the calculated density from the lattice parameters; and (3) the measured value from GC.

QSDs that shows dramatic changes attributable to the presence of octahedral cation vacancies; the above direct measurements of H by Raman spectroscopy (Figure 10); and a crystal-chemical analysis of the controlling factors of the *a* and *b* lattice parameters that allows one to deduce the influence of the vacancies, as distinct from the effects of cation exchange and changing average octahedral cationic charge.

Characterization, quantification, and origin of ancillary Fe oxide phases. Figure 11 shows the total amounts of Fe oxide phases produced, from Mössbauer spectroscopy (Table 6), expressed as percentages of total Fe, *vs.* treatment temperature for 5 h treatments. The value of 1.0(5)% for sample 300-5-W-k is obtained by comparison of the thickness-corrected spectrum with those of the other samples, rather than by fitting. This is because the small amount makes the fitting difficult to stabilize, even though the sextet contribution is clearly seen in expanded views such as that illustrated in Figure 4c. The spectra of samples heated below 300°C and of the original unoxidized sample did not show any detectable sextet contributions. This figure shows no appreciable Fe oxide formation up to

the point of complete depletion of OH, occurring between 350 and 370°C (Figures 8c and 10), followed by a steep increase of Fe oxide content on increasing the treatment temperature, up to the point of complete annite oxidation, occurring between 400 and 450°C (Figure 7), beyond which the Fe oxide content is stable at an average value of 11.3(5)%. The latter number is significant because the theoretical value, based on assuming that the oxybiotite reaction has proceeded to completion and that there were no vacancies present in the starting unoxidized annite, is $\frac{1}{9} = 11.1\%$. This prediction is not affected by the fact that some ferric Fe (and associated OH deficiency) is present in the starting unoxidized annite. The observed value of 11.3(5)% can be taken both as corroborating evidence for an absence of vacancies in the starting unoxidized annite and as strong evidence for the proposed combined effects of the oxybiotite and vacancy reactions. The region of steep increase in Fe oxide content (between $T_{TR} \gtrsim 350°C$ and $T_{TR} \lesssim 450°C$) should be interpreted as the region where the vacancy reaction (reaction 2) is dominant.

The total amounts of Fe oxide, from Mössbauer spectroscopy (Table 6, Figure 11), are comparable to the es-
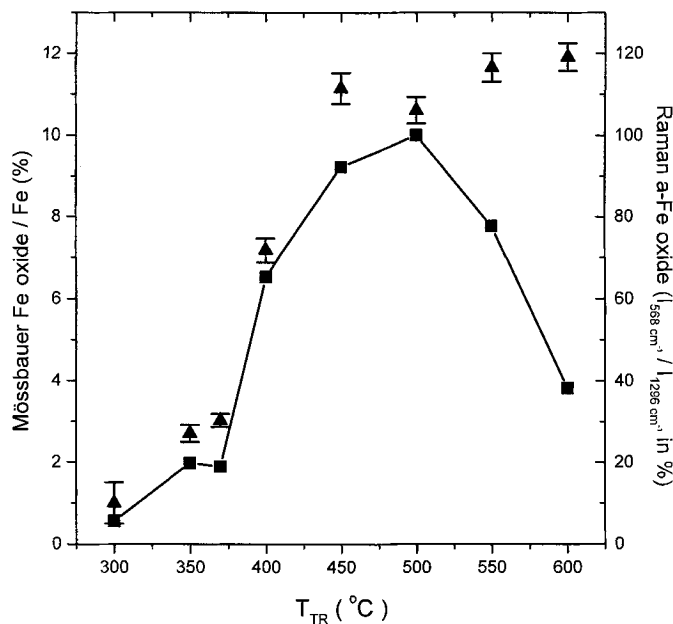
Figure 11. Total Fe oxide phase population from Mössbauer spectroscopy (triangles with error bars), expressed as a fraction of total Fe in % (left scale), and amount of poorly crystalline Fe oxide phase detected by Raman spectroscopy (squares, joined by line segments), expressed as the ratio (in %, right scale) of the integrated Raman intensities of the lines at 568 cm^{-1} (main poorly crystalline Fe oxide band) and at 1296 cm^{-1} (selected normalization band), *vs.* treatment temperature for 5 h treatments. The saturation amount of total Fe oxide measured by Mössbauer spectroscopy is in agreement with the theoretical value of 11.1% for an ideal ferrioxyannite vacancy concentration of $\frac{1}{9}$ per octahedral site.

timated quantitative amounts of hematite from pXRD (Table 2). The actual sextet contributions (*e.g.* Figure 4c) have significant structure, where classic hematite sextet contributions are clearly resolved (with $z \approx 3.5$ mm/s, narrow lines, and $\epsilon \approx -0.1$ mm/s; Table 5) in addition to smaller splitting and broader sextet contributions that cannot be attributed unambiguously to a particular well crystalized Fe oxide phase. The latter contributions are consistent with poorly crystalline magnetite (Murad and Johnston, 1987), poorly crystalline maghemite (Murad and Johnston, 1987; Da Costa *et al.,* 1998), and small-particle hematite-like phases (Dang *et al.,* 1998) and might be expected to produce relatively broad pXRD reflections that are difficult to detect (*e.g.* Kodama *et al.,* 1977). They are also detected as a poorly crystalline Fe oxide phase in our Raman spectroscopy measurements (see below). Note that our analysis of the Mössbauer spectra treats all Fe oxide sextet contributions as one continuous HFD, in order to simplify the analysis and stabilize the fitting. The resulting HFDs show the distinct well crystallized hematite and other Fe oxide contributions. This is shown in Figure 12, where the HFDs for samples treated for 5 h at temperatures of 450–600°C are compared. The sharp peak due to well crystallized hematite can be clearly distinguished from the broad hump due to the poorly crystalline oxides. It is interesting to note (Figure 12) that the latter oxides are progressively transformed to hematite, as the treatment temperature is

increased, suggesting that they are the first metastable products of the oxidation reaction involving Fe supplied by the vacancy mechanism. The inset shows the well crystallized hematite/Fe oxide fraction as a function of treatment temperature. This fraction (~25%), in combination with the total amount of Fe oxide deduced from the Mössbauer spectra (~11% of total Fe, Table 6), is significantly smaller than the amounts of hematite deduced from pXRD. The latter weight ratios (Table 2) correspond to fractions of total Fe in hematite in the range 9–17%. These fractions increase with increasing treatment temperature, as do the Mössbauer data shown in Figure 12 although the latter numbers are smaller. Assuming a different but reasonable value of RIR for annite of 7.0 (instead of 4.0, see above) yields fractions of total Fe in hematite from the pXRD weight ratios (Table 2) in the range 5–11%. The above considerations suggest that the poorly crystalline Fe oxide fractions seen by both Mössbauer spectroscopy (Figures 4c, 12) and Raman spectroscopy (described below) are predominantly small-particle hematite-like phases that give hematite-like pXRD patterns (Dang *et al.,* 1998).

Raman spectroscopy provides supporting evidence of the above interpretations concerning the ancillary Fe oxide phases. A doublet of relatively broad peaks that spans the wavenumber range 500–700 cm^{-1}, with a more intense band (by a factor of ~4) centered at 560 cm^{-1} and a weaker shoulder band at 660 cm^{-1},
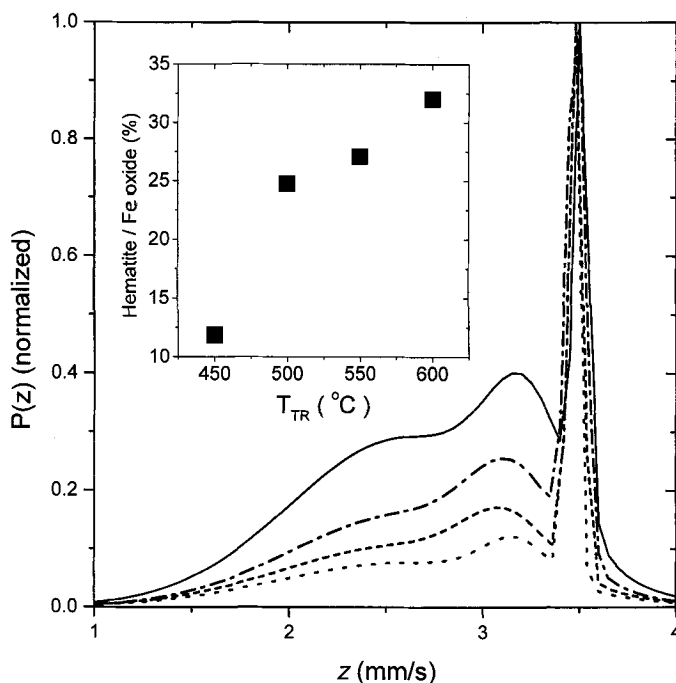
Figure 12.   Normalized HFDs for the samples treated for 5 h at 450 (solid line), 500 (dash-dot line), 550 (dash-dash line), and 600°C (dot-dot line). The sharp contribution at $z = 3.5$ mm/s is due to hematite whereas the broad contribution in the range $z = 1.5$–3.5 mm/s is attributed to an unidentified poorly crystalline Fe oxide phase. Corresponding fit parameters are given in Table 5. The inset shows the fraction of all Fe oxide that is hematite as a function of treatment temperature.

appears at the higher treatment temperatures (starting at 300°C and having maximum relative integrated intensity at 500°C, see Figure 5). This doublet feature is unambiguously attributed to the same poorly crystalline Fe oxide phase that is detected by Mössbauer spectroscopy and described above since: (1) it has a treatment temperature dependence of its normalized integral intensity that closely follows the treatment temperature dependence of the total Fe oxide contribution measured by Mössbauer spectroscopy up to 500°C, as shown in Figure 11; and (2) it has a spectral signature, in particular the main peak at 560 cm^{-1}, that cannot be related to the Raman spectra of known well crystallized Fe oxides and oxyhydroxides (hematite, maghemite, goethite, lepidocrocite, δ-FeOOH, magnetite and wüstite (de Faria *et al.,* 1997)). Figure 13 shows an expanded view of the poorly crystalline oxide feature in the Raman spectrum of sample 500-5-W-m. Figure 13 also allows one to observe another feature that only occurs at the highest treatment temperatures, in the form of a band that spans the wavenumber range 270–330 cm^{-1}. This band is centered at the position of the strongest Raman peak in the Raman spectrum of hematite (de Faria *et al.,* 1997) and it has a treatment temperature dependence that closely matches that of the hematite contribution measured by Mössbauer spectroscopy (inset of Figure 12), in that it is not detected at $T_{TR} \leq 450°C$ and has an almost

constant value of its normalized integral intensity at $T_{TR} = 500$–600°C. It is therefore unambiguously attributed to hematite. Since we know from Mössbauer spectroscopy (Figure 12) that at $T_{TR} = 500$–600°C, approximately one quarter of the Fe oxides are in the form of well crystallized hematite, we conclude from Figures 5 and 13 that the effective Raman activity strength for well crystallized hematite is much weaker in this application than that of the poorly crystalline oxide phase. The drop in the Raman signal, at the highest treatment temperatures of the poorly crystalline phase (Figure 11) is understood as a consequence of the oxide transformation towards well crystallized hematite.

It is important to verify the extent to which weight changes measured by TGA are consistent with the above interpretation of the oxidation mechanisms. Figure 14 shows TGA curves measured both in air and under dry N_2, at a heating rate of 20°C/min. It is noted that, after an initial, almost constant, weight region, a weight increase occurs in the temperature range from ~300 to ~600°C as temperature is increased. This weight increase has its maximum rate at 477(1)°C and is complete at 550°C, as can be ascertained from the derivative curve (not shown). It corresponds to an oxidation since it is absent from the TGA measurement done under N_2. The net magnitude of the weight increase, measured from the lowest point on the pre-oxidation plateau to the highest point above the max-
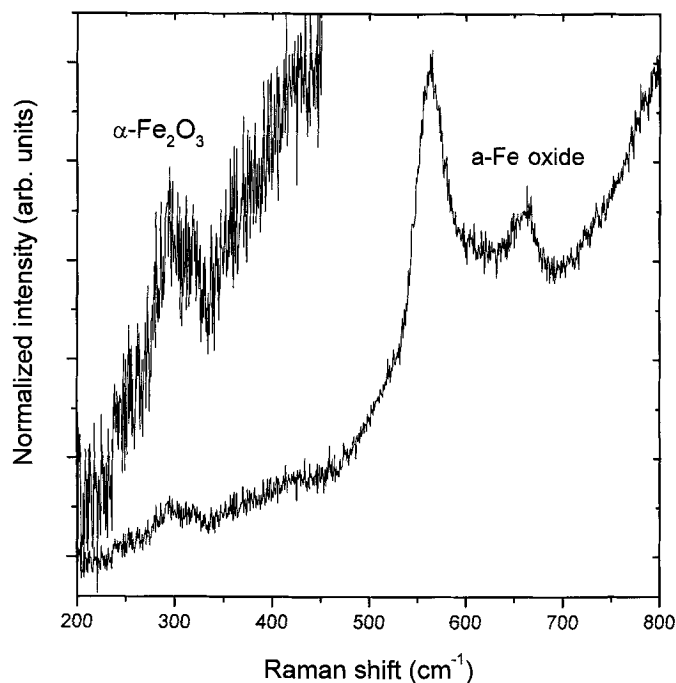
Figure 13.   Expanded view of the Raman spectrum for sample 500-5-W-m highlighting the poorly crystalline Fe oxide and hematite bands, labeled a-Fe oxide and α-Fe$_2$O$_3$, respectively. The region 200–450 cm^{-1} is further expanded vertically to emphasize the relatively weak hematite band.
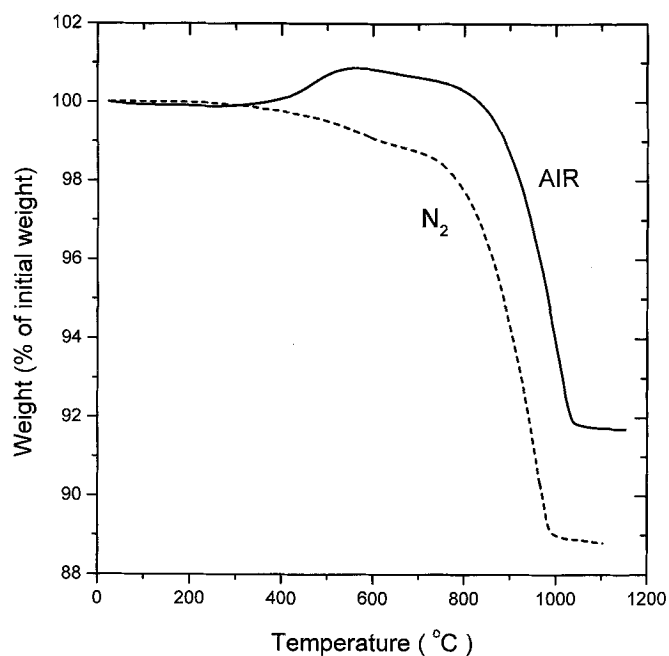

Figure 14.   TGA curves of vacancy-free synthetic annite, measured in air (solid line) and under dry N$_2$ (dashed line), at a heating rate of 20°C/min.

imum rate temperature, is 0.96% of the initial weight. A second TGA measurement under air was performed at the much slower heating rate of 2°C/min in another instrument. This measurement showed a similar weight increase event, starting at 350°C, ending at 500°C, having a point of maximum rate at 440(1)°C, and showing a net magnitude of the weight increase of 0.66–1.24% of the initial weight, depending on how the various buoyancy and other instrumental corrections are made. The latter measurement also showed a pre-oxidation event weight decrease of net magnitude ~0.25% of the initial weight, with point of lowest weight at ~350°C. A smaller pre-oxidation event decrease, of net magnitude ~0.06% of the initial weight and point of lowest weight at ~300°C, is seen in the 20°C/min experiment under air.

In comparing these TGA measurements, it is noted that a slower heating rate moves the oxidation event to lower temperatures, as expected. Given that the two mid-reaction points (477°C at 20°C/min and 440°C at 2°C/min) are not too different, we expect the TGA measurement performed at the slower heating rate to be a fair representation of the long-exposure-time thermal behavior of the sample and to be comparable to our 5 h exposure experiments. From this we conclude that Fe oxide formation starts at 350°C, in long-time exposures, in excellent agreement with our Mössbauer evaluation (Figure 11). In addition, the measured TGA net weight increase magnitudes are in quantitative agreement with the prediction from the proposed Fe oxide formation. For example, using an ideal annite structural formula (511.9 g/mole), transformation via the oxybiotite reaction to ideal oxyannite (509.9 g/mole) gives a net decrease of 0.39% of the initial weight. If this is followed by formation of ideal ferrioxyannite (491.3 g/mole) and hematite (α-Fe_2O_3) *via* the vacancy reaction using ambient oxygen, then the calculated net magnitude of the weight increase, measured from the lowest point on the pre-oxidation plateau to the highest point after the maximum rate temperature, is 1.56% of the initial weight, in fair agreement with the measured values. The predicted step-wise increase due to oxidation relative to the initial baseline value (*i.e.* not counting the weight loss due to H loss via the oxybiotite reaction) is 1.17% of the initial weight.

We conclude that the Fe oxide formation seen by both Mössbauer spectroscopy and TGA are in agreement and that all of the structural Fe lost from the original annite sample is accounted for. By comparison, assuming that the vacancy reaction alone is responsible for all Fe oxidation in the annite sample leads to a predicted weight gain of 4.69% of the initial weight. Therefore, the overall complete oxidation of our annite sample: (1) cannot be due to the vacancy reaction alone because much more Fe oxide formation would be observed; (2) cannot be due to the oxybiotite reaction alone because oxidation would cease at Fe^{2+}/Fe = ⅓; and (3) is quantitatively consistent with both reactions occurring in turn and to completion, with the oxybiotite reaction exhausting itself first.

The measured TGA pre-oxide formation event decrease (0.25% at 2°C/min, 0.06% at 20°C/min) is smaller than the predicted value (0.39%) based on ideal annite. Using the correct starting stoichiometry given by reaction 5 gives a more realistic prediction of 0.33%, rather close to the value measured at the slower heating rate. The lower measured values may be due to the known slow kinetics of the oxybiotite reaction under air (Rancourt *et al.*, 1993a) or to low-temperature initial stage Fe oxide formation. Evidence for the latter effect is seen in Figure 11, at $T_{TR} \le 350°C$.

Differential thermal analysis also allows one to detect the formation of Fe oxides as a large exothermic event. This is shown in Figure 15 where the DTA signals measured under air and dry N_2 are compared. The large exothermic oxide-formation peak is only present in air and has its maximum at 487°C, close to the TGA point of maximum rate of 477°C, at the same heating rate. No other significant reactions are evident up to a sharp endothermic event at 776°C, followed by another sharp endothermic event at 1043°C (Figure 15). The latter events mark the beginning and end, respectively, of a large weight-loss (~8%) event seen in TGA (Figure 14), as temperature is increased at the same rate. These correspond to the breakdown of the mica structure and were not studied further. The high temperatures of occurrence of these breakdown events confirm our pXRD and Mössbauer observations that the final ferrioxyannite structure is stable to at least 600°C.

Spectroscopic detection of octahedral site vacancies. The above TGA, DTA and measurements of the amount of Fe oxide are consistent with initiation of substantial Fe-oxide formation occurring above 350°C, after all OH groups have been depleted by the oxybiotite reaction. We now present evidence that the formation of octahedral site vacancies in the oxidized annite closely follows the formation of these Fe oxides, as expected from the vacancy mechanism (reaction 2). Figure 16 shows three parameters ($\langle QS \rangle$, QS_{peak} and σ_{QSD}; Tables 4 and 6) which characterize the QSD of $^{[6]}Fe^{3+}$ in the annite samples, measured by Mössbauer spectroscopy, as functions of the treatment temperature, for 5 h exposures. For a given cation species with a given nearest-neighbor coordination number (*i.e.* in this case $^{[6]}Fe^{3+}$), the local QSs obtained from a QSD analysis are related directly to the local electronic charge distributions, which are in turn primarily determined by local distortions (*i.e.* the precise positions of the coordinating oxygen anions) and the amounts of binding charge transfers to or from these coordinating anions (*i.e.* the next nearest-neighbor cation species) (Rancourt, 1998). A next nearest-neighbor
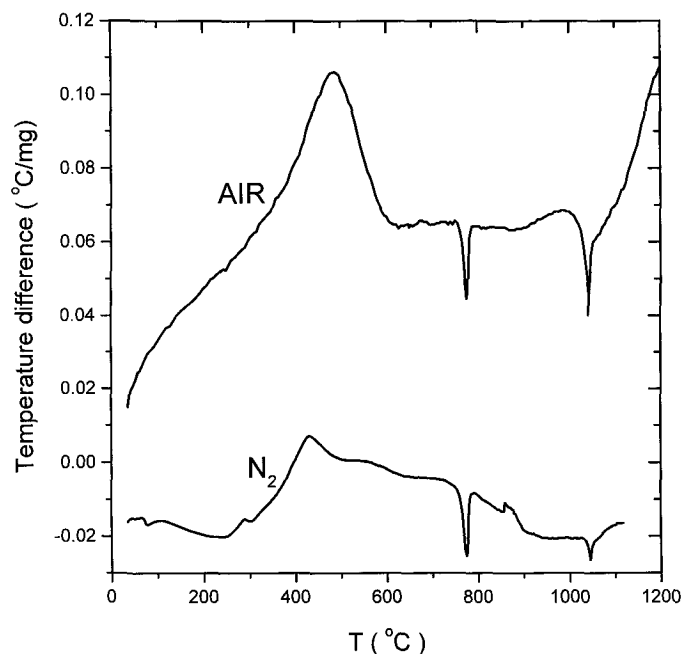
Figure 15.   DTA curves of vacancy-free synthetic annite, measured in air and under dry N_2, as indicated, at a heating rate of 20°C/min.

octahedral site vacancy, therefore, is expected to cause a large change in QS, relative to the symmetric octahedral site next nearest neighbor configuration where all six octahedral site next nearest neighbors are ferric Fe cations. Indeed, this change is expected to be much larger than changes due to varying the octahedral or tetrahedral next nearest-neighbor cation species, much larger than the change due to the loss of a neighboring OH group via the oxybiotite reaction, and certainly much larger than the difference in QS between the *cis* and *trans* octahedral sites of annite (Rancourt, 1994b). The presence of vacancies, therefore, is expected to be quite noticeable and easily recognized in the [6]Fe^{3+} QSDs. Figure 16 does show a dramatic change in QSD characteristics, where the average QS goes from a value of ~1.10 mm/s at $T_{TR} \leq 350°C$ to a value of ~1.45 mm/s at $T_{TR} \geq 450°C$. The region of change in QS coincides with the temperatures over which significant Fe-oxide formation occurs (Figure 11).

The changes in QSDs described above (Figure 16) are even more noticeable if one examines the QSDs themselves. This is shown in Figure 17 where several [6]Fe^{3+} QSDs are compared. One notes a distinct contribution in the QSDs that occurs at QS ~2.2 mm/s, that starts growing at ~350°C, and that saturates in amount at $T_{TR} \geq 450°C$. In view of the results above, this contribution can unambiguously be attributed to the presence of near-neighbor vacancies. Note, however, that the presence of vacancies is not a sufficient condition for the QS ~2.2 mm/s feature to occur. In muscovite, for example, the vacant *trans* sites of the

dioctahedral structure give rise to symmetric configurations of three vacancies around each cation occupying a *cis* site and the resulting [6]Fe^{3+} QSD has its main peak at QS ~1.0 mm/s, not at QS ~2.2 mm/s (Shabani *et al.,* 1998). Our observed QS ~2.2 mm/s feature probably corresponds to local [6]Fe^{3+} environments having one or two near-neighbor vacancies in non-symmetric configurations. In conclusion, the QS ~2.2 mm/s feature constitutes a direct spectroscopic signature of octahedral site vacancies whose intensity is strongly correlated with the presence of Fe oxides.

Oxybiotite and vacancy mechanisms give distinct crystal chemical behaviors. We end this section by describing another crystal chemical relation that shows a discontinuity in behavior as one goes from the region dominated by the oxybiotite reaction ($T_{TR} \leq 350°C$) to the region dominated by the vacancy reaction ($T_{TR} \geq 370°C$). Figure 18 shows *b vs.* the mean octahedral cation to oxygen bond length, [D], for two synthetic phlogopite–annite series described by Mercier (2001) and the annite and oxidized annite samples of the present study. [D] is calculated using the bond-length values for phyllosilicates given by Weiss *et al.* (1992), by averaging over the *cis* and *trans* octahedral sites, and using the nominal compositions and measured ferric/ferrous ratios from Mössbauer spectroscopy. We note the expected (*e.g.* Hazen and Wones, 1972; Radoslovich and Norrish, 1962; Radoslovich, 1962) linear relation that holds for the phlogopite–annite solid-solution and the striking deviation from this relation that
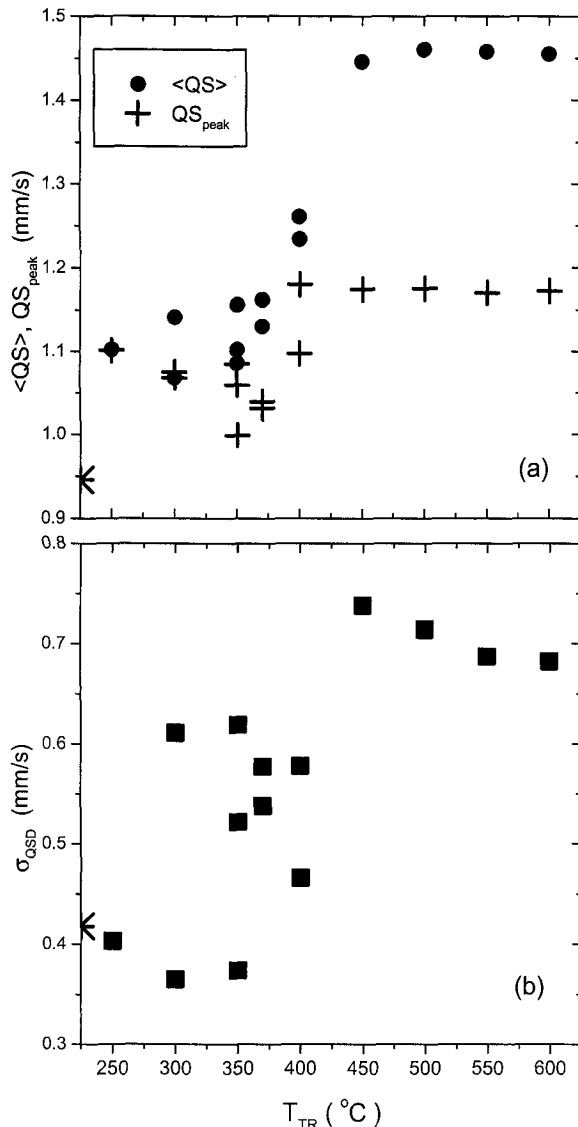
Figure 16.   Calculated $^{[6]}Fe^{3+}$ QSD parameters (Tables 4 and 6) as functions of the treatment temperature for 5 h treatments: (a) the average QS, $\langle QS \rangle$, and the QS of maximum probability density, QS_{peak}; (b) the standard deviation of the QSD, σ_{QSD}. The values for the unoxidized starting annite sample are shown (stars) on the left axes. For symmetric QSDs, one must have $\langle QS \rangle = QS_{peak}$.

corresponding to larger b values for given [D] values, relative to the phlogopite-annite relation. We tentatively interpret this as arising from larger octahedral flattening angles (ψ) caused by stronger intra-octahedral-sheet inter-cation electrostatic repulsion occurring as ferrous Fe is oxidized to ferric Fe. Some $\psi = $ constant predictions from crystal chemical considerations (equation 7, given below) are shown as a reference in Figure 18. We stress that other solid-solutions involving only divalent cations, such as Co-Mg and Ni-Mg, follow the Fe-Mg relation (Mercier, 2001) whereas the oxidized annite samples present a dramatic deviation (Figure 18).

The other important feature in Figure 18 is that, on crossing from the oxybiotite region to the vacancy region, the initial linear relation of the annite–oxyannite series is abandoned for a decrease that has a slope more like that of the phlogopite–annite relation. There is a sudden break in the curve that occurs between 350 and 370°C, at the same treatment temperature where there is: a complete loss of H (Figure 10); a discontinuity in c (Figure 8c); the start of oxide formation weight gain as seen in TGA when performed with a sufficiently low heating rate; the start of significant Fe-oxide formation as seen by Mössbauer spectroscopy (Figure 11) and substantiated by pXRD (Table 2), and the start of a sudden increase in the $^{[6]}Fe^{3+}$ average QS (Figure 16) that is associated with a QSD feature (Figure 17) that is unambiguously attributed to vacancies. We tentatively interpret the larger slope of b vs. [D] in the oxyannite–ferrioxyannite region as a recovery to phlogopite-annite-like behavior that occurs because the vacancy reaction (reaction 2) does not change the average octahedral site cationic charge, unlike the oxybiotite reaction which increases it significantly. A break in b vs. [D] behavior at $350°C < T_{TR} < 370°C$ is present irrespective of the particular assumptions concerning stoichiometry (*i.e.* all vacancy mechanism, no vacancies, oxybiotite reaction acting alone at first and up to completion). It does not reflect a break in b vs. T_{TR} (Figure 8b) and it is not related to the break in c vs. T_{TR} (Figures 8c, 9). The break in behavior is real and points to a significant change in crystal chemistry that invalidates a linear dependence on the single parameter [D] over the entire range of ferric/ferrous ratios.

Particle-size effects and reaction inhomogeneity in the oxidation of annite

Given what is known about the kinetics of the oxybiotite reaction (Rancourt *et al.*, 1993a), we should not expect our quenched oxidized annite samples to be in near-equilibrium states. Their oxidations have been interrupted at various stages and the samples can only be expected to be uniform to the extent that the reactions are homogeneous and not diffusion limited. On the other hand, the starting material is remarkably uni-
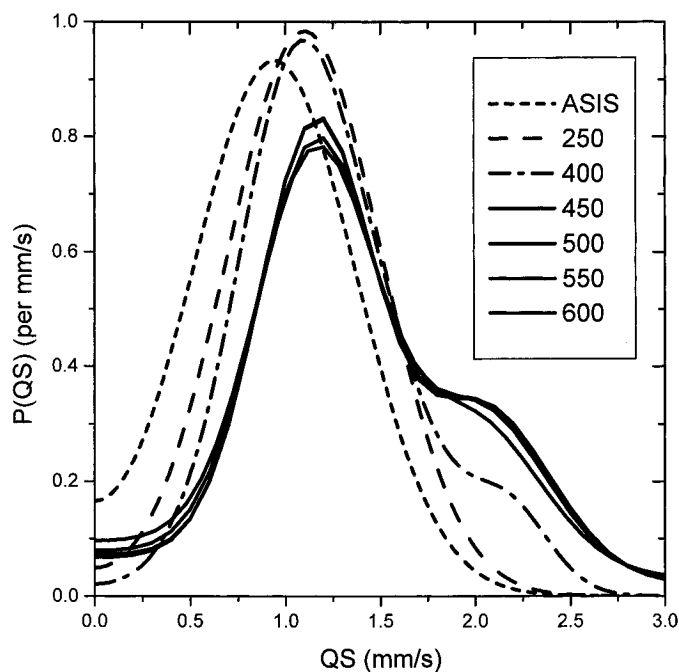
is exhibited by the annite-oxyannite-ferrioxyannite samples. Such a deviation occurs irrespective of any particular assumed stoichiometries of the oxidized annite samples. That is, any assumed combination of the oxybiotite and vacancy mechanisms gives a severe deviation such as the one illustrated in Figure 18. Given the results presented above, we have assumed annite-oxyannite stoichiometries at $T_{TR} \leq 350°C$ and oxyannite-ferrioxyannite stoichiometries at $T_{TR} \geq 370°C$. In the annite–oxyannite region, one obtains a linear relation but one having a much smaller slope and mostly

Figure 17. $^{[6]}Fe^{3+}$ QSDs for the unoxidized starting annite sample (ASIS) and for various oxidized annite samples (5 h treatments in air at the temperatures indicated (°C)). The ferrioxyannite samples ($T_{TR} \geq 450°C$) have a maximum amount of a component at QS $\approx$ 2.2 mm/s that is attributed to nearest-neighbor octahedral cation vacancies.
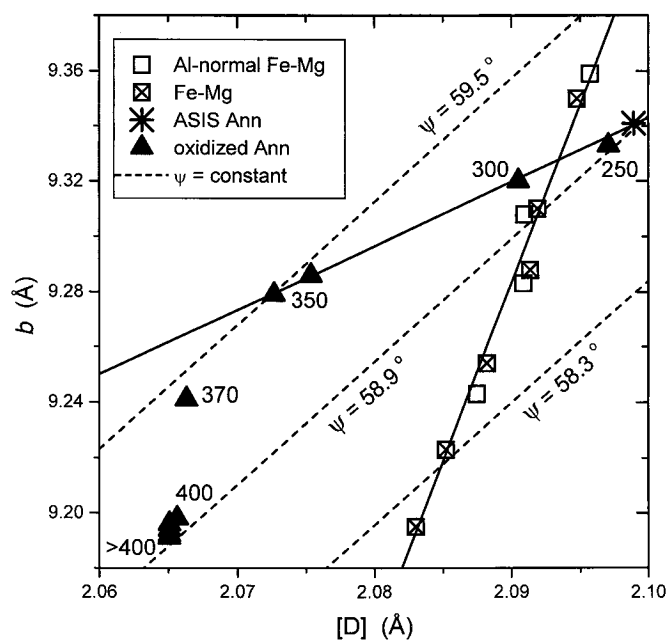

Figure 18. *b vs.* the mean octahedral cation to oxygen bond length [D] for the unoxidized starting annite sample and for the oxidized annite samples (5 h treatments in air at the temperatures indicated in °C), compared to the values for synthetic samples in the phlogopite–annite series (Mercier, 2001) and to three theoretical predictions corresponding to constant octahedral flattening angles (as indicated, dashed lines). The solid lines are guides to the eye.
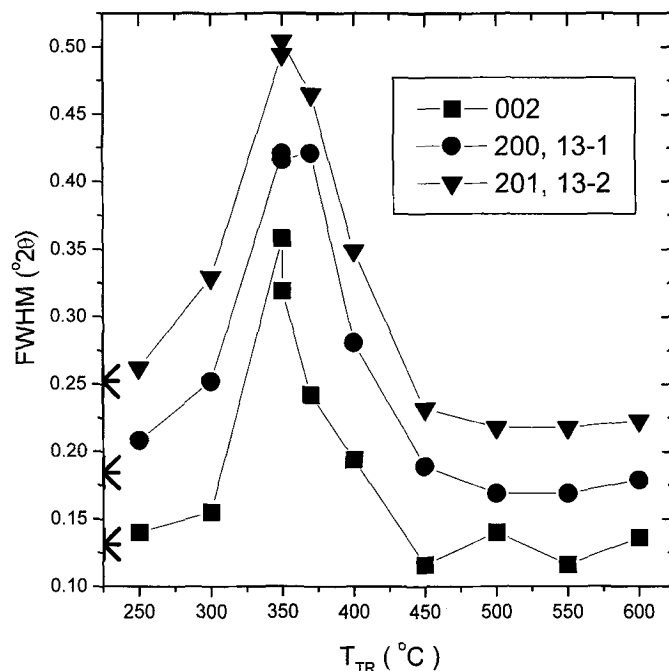
Figure 19. pXRD full widths at half maximum of reflections (as labeled) as functions of the treatment temperature for 5 h treatments. The values for the unoxidized starting annite sample are shown (stars) on the left axis.

form, with no detectable difference in lattice parameters between the different size-fractions (Table 1) and the S fraction being only slightly more oxidized than the L fraction, which is the same within error as the whole fraction W (Table 4). The Fe^{3+}/Fe ratio of the S fraction is ~2% of total Fe larger than that of the L fraction (Table 4).

We have compared the oxidation of the W and S fractions, performed under identical conditions (350°C, 5 h) and find that: (1) the amount of $^{[4]}Fe^{3+}$ is the same within experimental error, as expected; and (2) the amount of $^{[6]}Fe^{3+}$ is greater in the S fraction by ~15%, from ~50% in the whole sample to ~58% in the S fraction (Table 4). This suggests that diffusion does play an important role in the oxybiotite reaction, which is expected to dominate at this temperature, even with these clay-size particles, and it is consistent with our unpublished NRA data of H depth profiles in laboratory-oxidized biotite wafers in which surface depletion occurs with a decay length of ~1 μm. Nonetheless, the diffusion inhomogeneity effect is not so large and this allows the present study that compares various average properties.

Another measure of sample inhomogeneity can be obtained from pXRD peak widths. The peak widths of three reflections are shown in Figure 19, as functions of treatment temperature for 5 h oxidations. One notes that the samples having intermediate degrees of oxidation have the largest peak widths, suggesting that each such sample consists of domains having different degrees of oxidation whereas unoxidized samples (T_{TR}

≤ 250°C) and completely oxidized (ferrioxyannite) samples ($T_{TR} \geq$ 450°C) are uniform. The broadening is not a particle-size effect since the particle sizes do not change with heat treatment (SEM pictures, not shown) and all particles are too large to cause significant pXRD peak broadening. It is also unlikely that the broadening is a simple strain effect from cation disorder because both the starting annite and the resulting ferrioxyannite are expected to have significant cationic mixing and disorder yet do not show the anomalous broadening. Also, cation disorder in octahedral sites is not expected to cause such large broadening in 00l reflections as seen here, which we attribute to OH inhomogeneity. Indeed, the width of the 002 reflection drops significantly (as do the widths of all 00l reflections, not shown) beyond the postulated pillaring collapse transition that occurs between 350 and 370°C, relative to the widths of hkl-type reflections that do not show this sudden decrease in width (Figure 19).

Given the inhomogeneities described above, one can ask whether they are not so large as to invalidate any attempt to use average properties. It is possible that the particle to particle or domain to domain differences are larger than the average S fraction to average L fraction differences. Here again, the pXRD peak widths are useful. The pXRD peaks of the samples with intermediate degrees of oxidation must not be simple bimodal superpositions of the annite and ferrioxyannite peaks, as in the case of a two-phase mixture. Instead, they must be unimodal peaks having
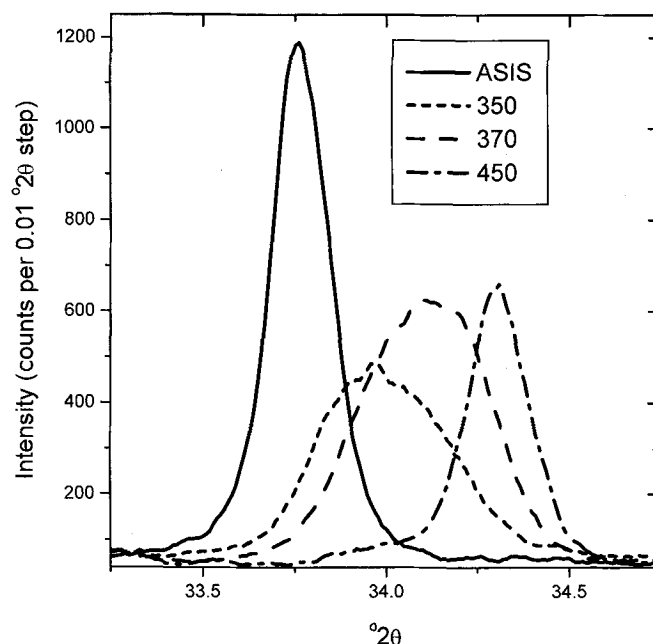
Figure 20.   pXRD patterns showing the 200 + 13-1 reflection of four samples: the unoxidized starting annite sample, and oxidized annite samples treated for 5 h in air at 350, 370 and 450°C, as indicated.

widths that are smaller than the peak-to-peak distances for the annite and ferrioxyannite peaks. This is indeed the case, as shown in Figure 20 for the 200 + 13-1 reflection.

Crystal chemical diagnostic test for vacancies in synthetic annite

In view of the results presented in this paper, we can be reasonably certain that our starting annite material was stoichiometric and did not contain octahedral site vacancies ($\square$/Oct <1%: XRF, NRA results, and Figure 10 inset) and that vacancies were not produced in significant concentrations in the samples oxidized in air for 5 h up to 350°C, where the oxybiotite reaction clearly dominated the oxidation of ferrous Fe. The b lattice parameter can be measured with accuracy and should, for a given set amount of [4]Fe^{3+} (and [6]Al^{3+}), depend on the degree of oxidation, measured by Fe^{2+}/Fe, both because [6]Fe^{3+} has a smaller cation radius than [6]Fe^{2+} and because of the effect that octahedral cationic charge probably has on octahedral flattening (Figure 18). The number of octahedral site vacancies must also affect b, though here we distinguish two extreme types of octahedral site vacancies that have very different effects. Type 1 vacancies are those that are created via the vacancy mechanism described by reaction 2 and that consequently have almost zero net predicted effect on b, whereas type 2 vacancies are those that arise from non-ideal stoichiometry by a mechanism that does not conserve octahedral cationic charge but balances it instead by adjusting the tetra-

hedral cationic charge. The second type of vacancy can occur when the synthesis material contains Fe and Al or Si-bearing impurity phases but only the first type of vacancy can occur if only Fe-bearing impurity phases (*i.e.* Fe oxides or Fe oxyhydroxides) are present. An absence of impurity phases implies that no vacancies are present. The main crystal chemical factors affecting b can be expressed conveniently via the following theoretical expression (Donnay *et al.*, 1964):

$$
\begin{aligned}
b = {} & 3\sqrt{3} \, \sin \psi [D] \\
= {} & 3\sqrt{3} \, \sin \psi [D(Fe^{2+}) - X\{D(Fe^{2+}) - D(Fe^{3+})\} \\
& - Y\{D(Fe^{2+}) - D(Al^{3+})\} \\
& + v_1\{D(\square) + 2D(Fe^{3+}) - 3D(Fe^{2+})\} \\
& + v_2\{D(\square) - D(Fe^{2+})\}]
\end{aligned}
\tag{7}
$$

where D(A) is the A–O bond length of octahedral site cation A, using the values for phyllosilicates of Weiss *et al.* (1992) averaged over *cis* and *trans* sites, X = [6]Fe^{3+}/Oct is the fraction of octahedral sites occupied by [6]Fe^{3+} that has been generated by the oxybiotite reaction, Y = [6]Al^{3+}/Oct is the fraction of octahedral sites occupied by [6]Al^{3+} that have arisen from [6]Fe^{3+} + [4]Al^{3+} $\rightleftharpoons$ [4]Fe^{3+} + [6]Al^{3+} exchange, v_1 = [6]$\square$(type 1)/Oct is the fraction of octahedral sites occupied by type 1 vacancies, and v_2 = [6]$\square$(type 2)/Oct is the fraction of octahedral sites occupied by type 2 vacancies. Given the relevant values of D(A) (D(Fe^{2+}) = 2.110 Å, D(Fe^{3+}) = 2.053 Å, D(Al^{3+}) = 1.919 Å, and D($\square$) =
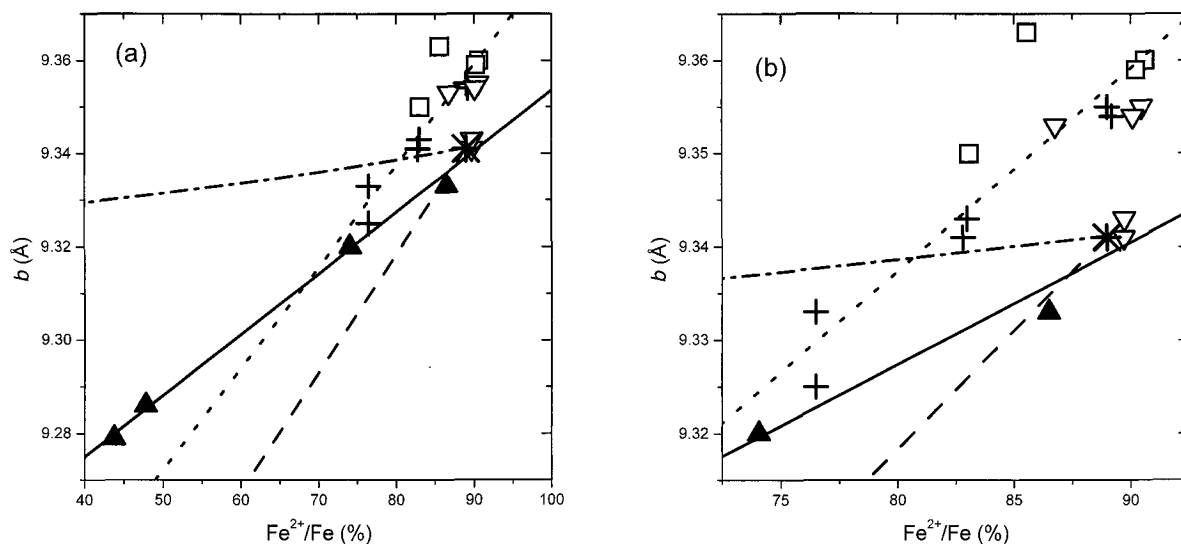
Figure 21.   *b vs.* Fe^{2+}/Fe values for several annite and oxidized annite samples, on large (a) and expanded (b) scales. Our oxidized annite samples 250-5-W-m, 300-5-W-m, 350-5-W-m and 350-5-W-k (Tables 1 and 4) are shown as filled triangles. The open triangles are for samples that are re-equilibrated ASIS material using the C-CH$_4$ buffer at various temperatures (Mercier, 2001). The open squares represent various annite samples that are known to contain impurity phases (Mercier *et al.*, 1996; Mercier, 2001). The unoxidized starting annite sample is located using a star. The solid line is the best line through our annite-oxyannite samples ($T_{TR} \leq 350°C$, 5 h treatments) and has the same meaning as the corresponding solid line in Figure 18. All points above this line are interpreted as corresponding to annite samples that contain vacancies. The dotted line is the best line through the data of Rebbert *et al.* (1995) data (crosses) and is intended as a guide to the eye. The dashed line is the prediction corresponding to equation 7 with $Y = 0.04$, $v_1 = v_2 = 0$, $\psi = 58.95°$, and only X variable (*i.e.* oxybiotite reaction acting alone). The dot-dashed line is the prediction corresponding to equation 6 with $Y = 0.04$, $X = 0.07$, $v_2 = 0$, $\psi = 58.95°$, and only v_1 variable (*i.e.* reaction 2 vacancy mechanism acting alone).

2.210 Å), one notes that the effect of type 1 vacancies is almost nil whereas type 2 vacancies are predicted to have a large effect on *b*.

We compare various predictions given by equation 7 with our measured data and with the data of Rebbert *et al.* (1995) and Mercier *et al.* (Mercier, 1996, 2001; Mercier *et al.*, 1996, 1999) in Figure 21, where *b* values are plotted *vs.* Fe^{2+}/Fe. The solid line represents a best line fit to our measured data for 5 h treatments with $T_{TR} \leq 350°C$. The dotted line represents the best line fit to the data of Rebbert *et al.* (1995). The prediction corresponding to equation 7 with $Y = 0.04$, $v_1 = v_2 = 0$, $\psi = 58.95°$, and only X variable (*i.e.* oxybiotite reaction acting alone in our starting annite sample), is shown as a dashed line. Here, the particular value of the octahedral flattening angle ψ is chosen to give agreement with our starting annite. As discussed in relation to Figure 18, we suggest that this prediction (dashed line) has a larger slope than the best line through our data mostly because the increased octahedral cationic charge arising from the progression of the oxybiotite reaction causes the octahedral flattening angle to increase whereas the prediction is for constant ψ. Reducing the average octahedral cation radius at constant octahedral cationic charge causes a reduction in ψ (Figure 18). The prediction corresponding to equation 7 with $Y = 0.04$, $X = 0.07$, $v_2 = 0$, $\psi =$

$58.95°$, and only v_1 variable (*i.e.* reaction 2 vacancy mechanism acting alone with initial v_1 of starting annite equal to zero), is shown by a dot-dashed line. Predictions where only v_2 is a variable correspond to large increases in *b* as v_2 increases (not shown). The large values of *b* shown in Figure 21 that occur above the solid line are consistent with $v_2 =$ [6]$\square$(type 2)/Oct $\sim 10\%$.

Given that our samples are initially vacancy free, as amply demonstrated by our measurements (at most $\square$/ Oct $\sim 1\%$: NRA results and Figure 10 inset), Figure 21 then shows that the samples of Rebbert *et al.* (1995) and those samples of Mercier *et al.* that are known to contain impurity phases must contain type 2 vacancies and therefore are not stoichiometric. Here, by non-stoichiometric we mean Al/Si/Fe $\neq$ 1/3/3, irrespective of cationic distributions between tetrahedral and octahedral sites. This is consistent with the impurity phases (4–7% by volume of sanidine and magnetite and/or fayalite) reported by Rebbert *et al.* (1995). A graph such as that illustrated in Figure 21 therefore provides both a sensitive detection of type 2 vacancies and a characteristic signature (via the slope) of when the oxybiotite reaction acts alone.

One might tentatively ascribe the larger slope of the line through the data of Rebbert *et al.* (1995) (Figure 21) as evidence for the vacancy mechanism (reaction 2) in

samples that might have constant type 2 vacancy contents, since it is closer to the larger slopes of octahedral site charge preserving reactions or substitutions (Figure 18). This would be tenuous, however, given the large effect that type 2 vacancies are expected to have on b (equation 7) and the unknown ratios of type 1 and type 2 vacancies. One can only conclude that it would be very difficult to discern the oxybiotite (reaction 1) and vacancy (reaction 2) mechanisms in samples that contained uncontrolled amounts of type 2 vacancies. This is particularly true given that the type 1 and type 2 vacancies that we have described represent extremes of vacancy behavior and that the true situation involving competition with impurity phases can involve intermediate vacancy formation mechanisms. Rebbert *et al.* (1995) stated that their data "on the synthetic iron biotite specimens rule out the oxybiotite substitution as the fundamental mechanism for biotite oxidation in these end-member systems" and further suggested that a reaction that couples vacancy formation and Fe oxidation must play a key role. We agree with Rebbert *et al.* (1995) if they are stating that usual hydrothermal synthesis of annite involves both impurity phases and vacancies and that the latter are affected by the experimentally imposed hydrogen fugacity (as is Fe^{3+}/Fe) and other synthesis variables. However, our data strongly support the conclusion that the dominant Fe oxidation mechanism at equilibrium in stoichiometric annite is the oxybiotite reaction (reaction 1). Our stoichiometrically near-ideal and impurity-phase-free starting annite sample and some of the re-equilibrated annite samples of Mercier *et al.* (1996, 1999) (of the same starting annite material) have Fe^{3+} populations that are quantitatively understood in terms of the oxybiotite reaction. The starting annite sample can also be re-equilibrated at conditions where impurity phases form and only such samples have vacancies, and Fe^{3+} populations that are not understood in terms of the oxybiotite reaction alone (Mercier *et al.*, 1996, 1999).

Sequence of oxidation reactions and minimization of free energy

We have observed that, in heating our vacancy-free synthetic annite sample to progressively higher temperatures in air, there is a definite sequence where mainly the oxybiotite reaction acts first and to completion, followed by the vacancy reaction (reaction 2). Similar observations of this sequence have been made previously. Vedder and Wilkins (1969) found that the first stage of thermal decomposition of a natural biotite sample (Fe/Oct = 0.16) was H loss (oxybiotite reaction) and that it was followed by dehydroxylation. This is consistent with all of the Fe being oxidized by the oxybiotite reaction, without the vacancy reaction being required for further oxidation as would be the case in more Fe-rich samples. All authors who have studied thermal decomposition of biotite in air or in vacuum (Farmer *et al.*, 1971; Ferrow, 1987; Güttler *et al.*, 1989; Hogg and Meads, 1975; Ivanitskiy *et al.*, 1975; Rancourt *et al.*, 1993a; Rimsaite, 1970; Robert, 1971; Sanz *et al.*, 1983; Tricker *et al.*, 1976; Vedder and Wilkins, 1969) have found the first Fe oxidation reaction to be the oxybiotite reaction. Farmer *et al.* (1971) concluded that the vacancy reaction (reaction 2) only occurred at higher temperatures than the temperatures where the oxybiotite reaction acted and only in biotites that were sufficiently Fe rich. In agreement with this, Robert (1971) observed that F-rich biotite could retain a significant fraction of its original $^{[6]}Fe^{2+}$ far beyond the temperatures at which the oxybiotite reaction acted (his Figure 10).

We have also presented evidence (Figure 21 and associated discussion) that vacancies are only involved when they are imposed by inter-phase competition for cations. Under sufficiently reducing conditions, the key question is whether a stoichiometric mixture of starting materials (including corrections for equilibrium concentrations of cationic species in solution) can, in an ideal hydrothermal synthesis where pressure, temperature and hydrogen fugacity are controlled, lead to octahedral site vacancy-free annite at equilibrium, or if only a multi-phase field exists where there must be both octahedral vacancies and another Fe-bearing phase, consistent with the vacancy reaction producing enough Fe^{3+} (in cooperation with the $^{[6]}Fe^{3+} + ^{[4]}Al^{3+} \rightleftharpoons ^{[4]}Fe^{3+} + ^{[6]}Al^{3+}$ exchange) to reduce sufficiently the octahedral-tetrahedral sheet lateral extension mismatch. The latter position would be opposite to the simple view that one can understand the required ferric Fe content of annite without requiring octahedral site vacancies (*e.g.* Hazen and Wones, 1972, 1978; Mercier *et al.*, 1996, 1999) and would be contrary to all experimental thermodynamic studies that find a large single-phase annite field to exist in the equilibrium phase diagram, without requiring the existence of a vacancy-bearing end-member (*e.g.* Benisek *et al.*, 1996; Chou, 1997; Cygan *et al.*, 1996; Dachs, 1994; Dachs and Benisek, 1997; Eugster and Wones, 1962). If we accept the existence of a vacancy-free annite field at low oxygen fugacity (*i.e.* if we accept the existence of vacancy-free annite as a possible equilibrium phase) then, under less reducing conditions, the question becomes: as oxygen fugacity is increased, does a multi-phase (vacancy-bearing annite + Fe oxide) field develop that replaces the single-phase (vacancy-free annite) field, or is the presence of vacancy-bearing oxidized annite in synthesis products simply an artifact of non-ideal conditions and/or incorrectly positioned field boundaries and incomplete reactions? Using starting stoichiometries that do not correspond to ideal vacancy-free annite of course leads to separate questions related to varying the chemical potentials for the various cations and here, clearly, when annite is one of

the equilibrium phases it may be forced to have both non-annite stoichiometric ratios of cation occupancies and vacancies.

We believe the debate regarding vacancies in biotite (or annite) can be resolved as follows. If the set availabilities of all cations (that are imposed by the bulk composition) and the availabilities of the anions (that are effectively controlled by hydrogen fugacity in the presence of water) are such that a phase other than biotite can be formed that has a lower free energy per Fe atom (*i.e.* a lower Fe chemical potential) than does biotite then this phase will scavenge Fe from the biotite structure in a way that is limited only by availability of its other required constituents. As a result, biotite will often have octahedral site vacancies. If this occurs via the vacancy mechanism described by reaction 2, then hydrogen fugacity does not play a role on the biotite side but only intervenes via its affect on the stability of the competing phase. On the other hand, if the availabilities of cations are such that competing phases are not produced at equilibrium then the biotite will be vacancy free (within the limit set by entropy requirements) and will adjust its degree of oxidation according to the prevailing hydrogen fugacity by the reaction that allows it to have the lowest possible free energy. This reaction is the oxybiotite reaction since the vacancy reaction would require the formation of another Fe-bearing phase and does not have a coupling to hydrogen. A sufficiently large oxygen fugacity, however, will eventually make a scavenging Fe oxide phase viable in comparison to Fe^{2+}-bearing biotite, but then the system has left the single-phase stability field of biotite and has entered the adjacent sanidine ($KAlSi_3O_8$) plus magnetite (Fe_3O_4) field (Benisek *et al.*, 1996; Chou, 1997; Cygan *et al.*, 1996; Dachs, 1994; Dachs and Benisek, 1997; Eugster and Wones, 1962). We conclude that the vacancy mechanism is controlled by Fe chemical potentials (as reaction 2 clearly indicates) that are only affected by hydrogen fugacity via a competing phase and that it is therefore only operative in a multi-phase situation whereas the oxybiotite reaction is controlled directly by hydrogen fugacity and is the relevant reaction in single-phase syntheses. The alternative would be to abandon the possibility that vacancy-free annite can have a stability field under ideal hydrothermal synthesis conditions using ideal starting cationic proportions.

These ideas are consistent with the observed sequence of oxidation reactions in the thermal oxidation of biotite. The most readily available electrons are those supplied by H via the oxybiotite reaction. The $^{[6]}Fe^{3+}$ cations thereby produced are very similar to the $^{[6]}Fe^{3+}$ cations of competing Fe oxide phases and there is no significant driving force (*i.e.* difference in Fe chemical potential) to expel them. On the other hand, there will be a significant difference in Fe chemical potential between any remaining $^{[6]}Fe^{2+}$ (after the oxy-

biotite reaction has exhausted itself) and $^{[6]}Fe^{3+}$. The vacancy mechanism provides an easy channel to level this difference, without requiring tetrahedral site cationic charge modification or the associated need to exchange tetrahedral cations with competing phases, a high barrier process given the strength of tetrahedral bonds.

In other words, during thermal oxidation of biotite on laboratory time scales, although none of the products of any of the proposed reactions represent equilibrium under the experimental treatment conditions and although at most, metastable phases (such as ferrioxyannite) are produced, the following link exists between the thermal oxidation reaction sequence and thermodynamic stability under hydrothermal synthesis conditions. The oxybiotite reaction occurs first during thermal oxidation because it has faster kinetics. It has faster kinetics primarily because it has a lower bottleneck activation barrier. In general, the height of an activation barrier is greater the greater the difference in specific free energies between the starting and product states, because phases having more different free energies usually require more elaborate reconstructions to be transformed into each other. This means that the sequence of thermal oxidation reactions (which holds for biotite samples that contain significant amounts of vacancies) implies that vacancy-free annite and oxyannite have closer free energies than do vacancy-free annite and vacancy-bearing annite. This, in turn, ensures that, within the stability field of annite and even if one is under conditions that require vacancies (such as a bulk Fe stoichiometric deficiency), the reaction that responds to changing hydrogen (or oxygen, via the water stability constant) fugacity must be the oxybiotite reaction, rather than a vacancy reaction. The vacancy mechanism becomes a response to changing hydrogen fugacity only outside the single-phase stability field of annite, where a competing oxide phase is either an equilibrium phase or an intermediary metastable phase on the way to a multi-phase equilibrium.

ACKNOWLEDGMENTS

REFERENCES

Appleman, D.E. and Evans Jr., H.T. (1973) Indexing and least-squares refinement of powder diffraction data. *Geological Survey Computer Contribution*, **20**, 1–26.

Benisek, A., Dachs, E., Redhammer, G., Tippelt, G. and Amthauer, G. (1996) Activity-composition relationship in Tschermak's substituted Fe biotites at 700°C, 2 kbar. *Contributions to Mineral and Petrology*, **125**, 85–99.

Borggaard, O.K., Lindgreen, H.B. and Mørup, S. (1982) Oxidation and reduction of structural iron in chlorite at 480°C. *Clays and Clay Minerals*, **30**, 353–363.

Bouda, S. and Isaac, K.P. (1986) Influence of soil redox conditions on oxidation of biotite. *Clay Minerals*, **21**, 149–157.

Brindley, G.W. and Lemaitre, J. (1987) Thermal, oxidation and reduction reactions of clay minerals. Pp. 319–370 in: *Chemistry of Clays and Clay Minerals* (A.C.D. Newman, editor). Monograph **6**, Mineralogical Society, London.

Carter, G.F., Margrave, J.L. and Templeton, D.H. (1952) A high-temperature crystal modification of KO_2. *Acta Crystallographica*, **5**, 851.

Chou, I.-M. (1997) The use and misuse of the fH_2 sensors: a discussion of the paper by Dachs (1994). *Contributions to Mineral and Petrology*, **128**, 302–305.

Chung, F.H. (1974a) Quantitative interpretation of X-ray diffraction patterns of mixtures. I. Matrix-flushing methods for quantitative multicomponent analysis. *Acta Crystallographica*, **7**, 519–525.

Chung, F.H. (1974b) Quantitative interpretation of X-ray diffraction analysis of mixtures. II. Adiabatic principle of X-ray diffraction analysis of mixtures. *Journal of Applied Crystallography*, **7**, 526–531.

Clowe, C.A., Popp, R.K. and Fritz, S.J. (1988) Experimental investigation of the effect of oxygen fugacity on ferric-ferrous ratios and unit-cell parameters of four natural clinoamphiboles. *American Mineralogist*, **73**, 487–499.

Cygan, G.L., Chou, I.-M. and Sherman, D.M. (1996) Reinvestigation of the annite = sanidine + magnetite + H_2 reaction using the fH_2-sensor technique. *American Mineralogist*, **81**, 475–484.

da Costa, G.M., De Grave, E. and Vandenberghe, R.E. (1998) Mössbauer studies of maghemite and Al-substituted maghemites. *Hyperfine Interactions*, **117**, 207–243.

Dachs, E. (1994) Annite stability revised. 1. Hydrogen-sensor data for the reaction annite = sanidine + magnetite + H_2. *Contributions to Mineralogy and Petrology*, **117**, 229–240.

Dachs, E. and Benisek, A. (1997) Annite stability revised: hydrogen-sensor data for the reaction annite = sanidine + magnetite + H_2: additional results and reply to Chou. *Contributions to Mineralogy and Petrology*, **128**, 306–311.

Dang, M.-Z., Rancourt, D.G., Dutrizac, J.E., Lamarche, G. and Provencher, R. (1998) Interplay of surface conditions, particle size, stoichiometry, cell parameters, and magnetism in synthetic hematite-like materials. *Hyperfine Interactions*, **117**, 271–319.

Davis, B.L., Kath, R. and Splide, M. (1990) The reference intensity ratio: its measurement and significance. *Powder Diffraction*, **5**, 76–78.

de Faria, D.L.A., Silva, S.V. and de Oliveira, M.T. (1997) Raman microspectroscopy of some iron oxides and oxyhydroxides. *Journal of Raman Spectroscopy*, **28**, 873–878.

De Grave, E. and Van Alboom, A. (1991) Evaluation of ferrous and ferric Mössbauer fractions. *Physics and Chemistry of Minerals*, **18**, 337–342.

Donnay, G., Donnay, J.D.H. and Takeda, H. (1964) Trioctahedral one-layer micas. II. Predictions of the structure from composition and cell dimensions. *Acta Crystallographica*, **17**, 1374–1381.

Eugster, H.P. and Wones, D.R. (1962) Stability relations of the ferruginous biotite, annite. *Journal of Petrology*, **3**, 82–125.

Farmer, V.C., Russell, J.D., McHardy, W.J., Newman, A.C.D., Ahlrichs, J.L. and Rimsaite, J.Y.H. (1971) Evidence for loss of protons and octahedral iron from oxidized biotites and vermiculites. *Mineralogical Magazine*, **38**, 121–137.

Feeley, T.C. and Sharp, Z.D. (1996) Chemical and hydrogen isotope evidence for in situ dehydrogenation of biotite in silicic magma chambers. *Geology*, **24**, 1021–1024.

Feldstein, S.N., Lange, R.A., Vennemann, T. and O'Neil, J.R. (1996) Ferric-ferrous ratios, H_2O contents and D/H ratios of phlogopite and biotite from lavas of different tectonic regimes. *Contributions to Mineralogy and Petrology*, **126**, 51–66.

Ferrow, E. (1987) Mössbauer effect and X-ray diffraction studies of synthetic iron bearing trioctahedral micas. *Physics and Chemistry of Minerals*, **14**, 276–280.

Ferrow, E. (1990) The relation between c dimension and exchange components in micas. *Mineralogy and Petrology*, **43**, 23–25.

Ferrow, E. and Annersten, H. (1984) *Ferric iron in trioctahedral micas*. UUDMP Research Report no. 39. University of Uppsala, Uppsala, Sweden, 24 pp.

Gilkes, R.J., Young, R.C. and Quirk, J.P. (1972a) The oxidation of octahedral iron in biotite. *Clays and Clay Minerals*, **20**, 303–315.

Gilkes, R.J., Young, R.C. and Quirk, J.P. (1972b) Oxidation of ferrous iron in biotite. *Nature, Physical Science*, **236**, 89–91.

Goodman, B.A. and Wilson, M.J. (1973) A study of the weathering of a biotite using the Mössbauer effect. *Mineralogical Magazine*, **39**, 448–454.

Güttler, B., Niemann, W. and Redfern, S.A.T. (1989) EXAFS and XANES spectroscopy study of the oxidation and deprotonation of biotite. *Mineralogical Magazine*, **53**, 591–602.

Hazen, R.M. and Wones, D.R. (1972) The effect of cation substitutions on the physical properties of trioctahedral micas. *American Mineralogist*, **57**, 103–129.

Hazen, R.M. and Wones, D.R. (1978) Predicted and observed compositional limits of trioctahedral micas. *American Mineralogist*, **63**, 885–892.

Hellner, E. and Euler, R. (1957) Hydrothermal und röntgenographische untersuchungen an gesteinsbildenden mineralen—I. *Geochimica et Cosmochimica Acta*, **12**, 47–56.

Hogg, C.S. and Meads, R.E. (1975) A Mössbauer study of thermal decomposition of biotites. *Mineralogical Magazine*, **40**, 79–88.

Hubbard, C.R. and Snyder, R.L. (1988) RIR—Measurement and use in quantitative XRD. *Powder Diffraction*, **3**, 74–77.

Ivanitskiy, V.P., Kalinechenko, A.M., Matyash, I.V. and Khomyak, T.P. (1975) Mössbauer and PMR studies of oxidation and dehydroxylation in biotite. *Geochemistry International*, **12**, 1864–1871.

Kodama, H., McKeague, J.A., Tremblay, R.J., Gosselin, J.R. and Townsend, M.G. (1977) Characterization of iron oxide compounds in soils by Mössbauer and other methods. *Canadian Journal of Earth Sciences*, **14**, 1–15.

Lagarec, K. and Rancourt, D.G. (1998) *Recoil: Spectral analysis and data treatment software for Mössbauer spectroscopy.* http://www.science.uottawa.ca/phy/~recoil/.

Lalonde, A.E., Rancourt, D.G. and Ping, J.Y. (1998) Accuracy of ferric/ferrous determinations in micas: a comparison of Mössbauer spectroscopy and the Pratt and Wilson wet-chemical methods. *Hyperfine Interactions, 117,* 175–204.

Lanford, W.A. (1995) Nuclear reactions for hydrogen analysis. Pp. 193–204 in: *Handbook of Modern Ion Beam Materials Analysis* (J.R. Tesmer and M.A. Nastasi, editors). Materials Research Society, Pittsburg, Philadelphia.

Lanford, W.A., Trautvetter, H.P., Ziegler, J.F. and Keller, J. (1976) New precision technique for measuring the concentration versus depth of hydrogen in solids. *Applied Physics Letters, 28,* 566–568.

Lear, P.R. and Stucki, J.W. (1985) Role of structural hydrogen in the reduction and reoxidation of iron in nontronite. *Clays and Clay Minerals, 33,* 539–545.

McKeown, D.A., Bell, M.I. and Etz, E.S. (1999) Raman spectra and vibrational analysis of the trioctahedral mica phlogopite. *American Mineralogist, 84,* 970–976.

Mercier, P.H.J. (1996) An ^{57}Fe Mössbauer spectroscopy study of the effects of different equilibration temperatures and oxygen fugacity buffers on the Fe^{2+} and Fe^{3+} site populations in synthetic annite mica. M.Sc. thesis, University of Ottawa, Ottawa, Canada. 141 pp.

Mercier, P.H.J. (2001) Crystal chemistry of trioctahedral layer silicates: testing the limits of simple geometrical models (in preparation). Ph.D. thesis, University of Ottawa, Ottawa, Canada.

Mercier, P.H.J., Rancourt, D.G. and Berman, R.G. (1996) Aspects of the crystal chemistry of annite mica. P. 50 in: *Conference Proceedings, ICAME-95, Bologna,* SIF.

Mercier, P.H.J., Rancourt, D.G., Berman, R.G. and Robert, J.-L. (1999) Control of site populations, at synthesis, by intersheet differential thermal expansion in a 2:1 layer silicate. Pp. 221–228 in: *Clays for our Future* (H. Kodama, A.R. Mermut and J.K. Torrance, editors). *Proceedings of the 11th International Clay Conference, Ottawa, Canada.*

Murad, E. and Johnston, J.H. (1987) Iron oxides and oxyhydroxides Pp. 507–582 in: *Mössbauer Spectroscopy Applied to Inorganic Chemistry,* vol. II. Plenum Publishing Company, New York.

Ohta, T., Takeda, H. and Takéuchi, Y. (1982) Mica polytypism: similarities in the crystal structures of coexisting 1M and 2M1 oxybiotite. *American Mineralogist, 67,* 298–310.

Pajcini, V. and Dhamelincourt, P. (1994) Raman study of OH-stretching vibrations in kaolinite at low temperatures. *Applied Spectroscopy, 48,* 638–641.

Radoslovich, E.W. (1962) The cell dimensions and symmetry of layer-lattice silicates. II. Regression relations. *American Mineralogist, 47,* 617–636.

Radoslovich, E.W. and Norrish, K. (1962) The cell dimensions and symmetry of layer-lattice silicates. I. Some structural considerations. *American Mineralogist, 47,* 599–616.

Rancourt, D.G. (1989) Accurate site populations from Mössbauer spectroscopy. *Nuclear Instruments and Methods in Physics Research B (NIMB), 44,* 199–210.

Rancourt, D.G. (1994a) Mössbauer spectroscopy of minerals. I. Inadequacy of Lorentzian-line doublets in fitting spectra arising from quadrupole splitting distributions. *Physics and Chemistry of Minerals, 21,* 244–249.

Rancourt, D.G. (1994b) Mössbauer spectroscopy of minerals. II. Problem of resolving cis and trans octahedral Fe^{2+} sites. *Physics and Chemistry of Minerals, 21,* 250–257.

Rancourt, D.G. (1996) Analytic methods for Mössbauer spectral analysis of complex materials. Pp. 105–124 in: *Mössbauer Spectroscopy Applied to Magnetism and Materials Science.* Plenum Press, New York.

Rancourt, D.G. (1998) Mössbauer spectroscopy in clay science. *Hyperfine Interactions, 117,* 3–38.

Rancourt, D.G. and Ping, J.Y. (1991) Voigt-based methods for arbitrary-shape static hyperfine parameter distributions in Mössbauer spectroscopy. *Nuclear Instruments and Methods in Physics Research B (NIMB), 58,* 85–97.

Rancourt, D.G., Tume, P. and Lalonde, A.E. (1993a) Kinetics of the $(Fe^{2+} + OH^-)_{mica} = (Fe^{3+} + O^{2-})_{mica} + H$ oxidation reaction in bulk single-crystal biotite studied by Mössbauer spectroscopy. *Physics and Chemistry of Minerals, 20,* 276–284.

Rancourt, D.G., McDonald, A.M., Lalonde, A.E. and Ping, J.Y. (1993b) Mössbauer absorber thicknesses for accurate site populations in Fe-bearing minerals. *American Mineralogist, 78,* 1–7.

Rancourt, D.G., Christie, I.A.D., Royer, M., Kodama, H., Robert, J.-L., Lalonde, A.E. and Murad, E. (1994a) Determination of accurate $^{[4]}Fe^{3+}$, $^{[6]}Fe^{3+}$, and $^{[6]}Fe^{2+}$ site populations in synthetic annite by Mössbauer spectroscopy. *American Mineralogist, 79,* 51–62.

Rancourt, D.G., Christie, I.A.D., Lamarche, G., Swainson, I. and Flandrois, S. (1994b) Magnetism of synthetic and natural annite mica: ground state and nature of excitations in an exchange-wise two-dimensional easy-plane ferromagnet with disorder. *Journal of Magnetism and Magnetic Materials, 138,* 31–44.

Rancourt, D.G., Ping, J.Y. and Berman, R.G. (1994c) Mössbauer spectroscopy of minerals. III. Octahedral-site Fe^{2+} quadrupole splitting distributions in the phlogopite-annite series. *Physics and Chemistry of Minerals, 21,* 258–267.

Rancourt, D.G., Ping, J.Y., Boukili, B. and Robert, J.-L. (1996) Octahedral-site Fe^{2+} quadrupole splitting distributions from Mössbauer spectroscopy along the (OH, F)-annite join. *Physics and Chemistry of Minerals, 23,* 63–71.

Rebbert, C.R., Partin, E. and Hewitt, D.A. (1995) Synthetic biotite oxidation under hydrothermal conditions. *American Mineralogist, 80,* 345–354.

Redhammer, G.J. (1998) Characterisation of synthetic trioctahedral micas by Mössbauer spectroscopy. *Hyperfine Interactions, 117,* 85–115.

Redhammer, G.J., Beran, A., Schneider, J., Amthauer, G. and Lottermoser, W. (2000) Spectroscopic and structural properties of synthetic micas on the annite-siderophyllite binary: synthesis, crystal structure refinement, Mössbauer, and infrared spectroscopy. *American Mineralogist, 85,* 449–465.

Redhammer, G.J., Beran, A., Dachs, E. and Amthauer, G. (1993) A Mössbauer study and X-ray diffraction study of annites synthesized at different oxygen fugacities and crystal chemical implications. *Physics and Chemistry of Minerals, 20,* 382–394.

Rimsaite, J. (1970) Structural formulae of oxidized and hydroxyl-deficient micas and decomposition of the hydroxyl group. *Contributions to Mineralogy and Petrology, 25,* 225–240.

Robert, J.-L., Bény, J.-M., Bény, C. and Volfinger, M. (1989) Characterization of lepidolites by Raman and infrared spectrometries. I. Relationships between OH-stretching wavenumbers and compositions. *Canadian Mineralogist, 27,* 225–235.

Robert, M. (1971) Étude experimentale de l'évolution des micas (biotites). *Annales Agronomie, 22,* 43–93.

Ross, G.J. and Rich, C.I. (1974) Effect of oxidation and reduction on potassium exchange of biotite. *Clays and Clay Minerals, 22,* 355–360.

Royer, M. (1991) Site-specific Fe-57 Mössbauer recoilless fractions in true trioctahedral micas. MS thesis, University of Ottawa, Ottawa, Canada.

Sanz, J., Gonzales-Carreno, T. and Gancedo, R. (1983) On dehydroxylation mechanism of a biotite in vacuo and oxygen. *Physics and Chemistry of Minerals,* **9,** 14–18.

Schnatter, K.H., Doremus, R.H. and Lanford, W.A. (1988) Hydrogen analysis of soda-lime silicate glass. *Journal of Non-crystalline Solids,* **102,** 11–18.

Shabani, A.A.T., Rancourt, D.G. and Lalonde, A.E. (1998) Determination of cis and trans Fe^{2+} populations in 2M1 muscovite by Mössbauer spectroscopy. *Hyperfine Interactions,* **117,** 117–129.

Skogby, H. (1994) OH incorporation in synthetic clinopyroxene. *American Mineralogist, 79,* 240–249.

Skogby, H. and Rossman, G.R. (1989) OH^- in pyroxene: an experimental study of incorporation mechanism and stability. *American Mineralogist, 74,* 1059–1069.

Smith, G., Howes, B. and Hasan, Z. (1980) Mössbauer and optical spectra of biotite: a case for Fe^{2+}-Fe^{3+} interactions. *Physica status solidi (A),* **57,** K187–K192.

Speer, J.A. (1984) Micas in Igneous Rocks. Pp. 299–356 in: *Micas* (S.W. Bailey, editor). Reviews in Mineralogy, **13.** Mineralogical Society of America, Washington, D.C.

Takeda, H. and Ross, M. (1975) Mica polytypism: dissimilarities in the crystal structures of coexisting 1M and 2M1 biotite. *American Mineralogist, 60,* 1030–1040.

Tricker, M.J., Winterbottom, A.P. and Freeman, A.G. (1976) Iron-57 conversion-electron Mössbauer spectroscopic study of the initial stages of the oxidation of biotite. *Journal of Chemical Society—Dalton Transactions,* 1289–1292.

Vedder, W. and Wilkins, R.W.T. (1969) Dehydroxylation and rehydroxylation oxidation and reduction of micas. *American Mineralogist,* **54,** 482–509.

Veith, J.A. and Jackson, M.L. (1974) Iron oxidation and reduction effects on structured hydroxyl and layer charge in aqueous suspensions of micaceous vermiculites. *Clays and Clay Minerals,* **22,** 345–353.

Virgo, D. and Popp, R.K. (2000) Hydrogen deficiency in mantle-derived phlogopites. *American Mineralogist,* **85,** 753–759.

Volfinger, M., Robert, J.-L., Vielzeuf, D. and Neiva, A.M.R. (1985) Structural control of the chlorine content of OH-bearing silicates (micas and amphiboles). *Geochimica et Cosmochimica Acta,* **49,** 37–48.

Wada, N. and Kamitakahara, W.A. (1991) Inelastic neutron- and Raman-scattering studies of muscovite and vermiculite layered silicates. *Physical Review B,* **43,** 2391–2397.

Weiss, Z., Reider, M. and Chmielova, M. (1992) Information of coordination polyhedra and their sheets in phyllosilicates. *European Journal of Mineralogy,* **4,** 665–682.

Wilson, M.J. (1970) A study of weathering in a soil derived from a biotite-hornblende rock I. Weathering of biotite. *Clay Minerals,* **8,** 291–303.

Wones, D.R. (1963) Physical properties of synthetic biotites on the join phlogopite-annite. *American Mineralogist,* **48,** 1300–1321.

Ziegler, J.F. and Biersack, J.P. (2000) *The stopping and range of ions in matter.* SRIM computer software, version SRIM-2000.39.

Ziegler, J.F., Biersack, J.P. and Littmark, U. (1985) *The Stopping and Range of Ions in Solids.* Pergamon Press, New York. 321 pp.